X10: a magnetic cataclysmic variable with pole-switching accretion

by

Asma Ali Hassan Abbas Hattawi

A thesis submitted in partial fulfillment of the requirements for the degree of

Master of Science

Department of Physics
University of Alberta

Abstract

Cataclysmic variables (CVs) are binary stellar systems with a white dwarf (WD) and a companion star that is losing mass to the WD. When the magnetic field of the WD is strong enough, the accreting matter follows its magnetic field lines then falls near a magnetic pole. This leads to emission of radiation including X-rays. I analyzed Chandra X-ray data of the magnetic CV X10 in the star cluster 47 Tucannae. Analysis of the system's X-ray light curves shows a 4.185 ± 0.038 hour modulation, interpreted as the white dwarf (WD) spin period. The modulation also shows phase shifts around $\sim 165°$, which I interpret as a result of the accretion flow switching its trajectory between regions near two opposite WD magnetic poles. This implies a possible asynchronism between the WD spin and binary orbital periods. To investigate the two-accretion region scenario, I roughly constrained the system's geometry by simulating theoretical X-ray light curves and comparing them to observations. To investigate the degree of asynchronism, I constrained the orbital period of the system by analyzing the envelope patterns in the X-ray light curves, resulting in a range of possible orbital periods from ≈ 4.26 to ≈ 4.37 hours, that correspond to degrees of asynchronism from $\approx 1.76\%$ to $\approx 5.96\%$.

Preface

This thesis is original work by Asma Hattawi, with the help of Dr. Craig Heinke in data reduction, fitting the X-ray spectra and providing guidance and helpful suggestions throughout the project.

Acknowledgements

I would like to thank my adviser Dr. Craig Heinke for his continuous support and guidance. I would also like to thank my colleagues Pavan Hebbar and Yue Zhao for their help whenever I had questions about data processing or programming.

Contents

List of Tables

List of Figures

Chapter 1

Introduction

1.1 Definition and classification

Cataclysmic variables (CVs) are binary stellar systems with a white dwarf (WD) and a companion star that is typically a red dwarf (low mass Hydrogen-burning stars), in mutual orbit, and where the companion star is losing mass to the white dwarf. White Dwarfs are the result of the evolution of stars with masses lower than ~ 8 times the mass of our Sun, after they run out of their fuel for nuclear fusion. White dwarfs have high interior densities of around $\sim 10^6$ g/cm^3 and are held up by degeneracy pressure. They are slowly cooling down, with observed surface temperature ranging from a few thousand Kelvins to over a 100,000 K. (for a review on the physics of WDs, see Koester and Chanmugam, 1990).

In binary stellar systems, each companion has a potential well within which material is gravitationally bound to the star. This region is shaped like a tear, and is called the Roche lobe. Figure 1.1 shows an example 3 dimensional illustration of Roche lobes in a binary. And in every binary system, the point between the two stars along the line connecting their centres, where the Roche lobes of the two companions meet, is called the inner Lagrangian point. The inner Lagrangian point marks where the gravitational and centrifugal forces

of the two stars sum to zero. If one of the stars in the binary fills its Roche lobe, then material from its surface will end up flowing over the inner Lagrangian point, towards the other star. (for in-depth physics of close binaries, see Paczyński, 1971). In the case of cataclysmic variables, the red dwarf fills its Roche lobe and thus loses mass to the WD (Connon Smith, 2007).

The accreted matter coming from the atmosphere of the red dwarf is ionized. And since charged particles and strong enough magnetic fields interact (the charged particles are forced to follow magnetic field lines), then the way that the accreted matter moves towards the White Dwarf is dependent on the strength of the White Dwarf's magnetic field. The field sets the magnetospheric radius of the WD, within which the magnetic energy density $B^2/(8\pi)$ is higher than the kinetic energy density of the accreting material. Thus the accreting material cannot free-fall, and instead is channeled along the WD's magnetic field lines.

If the White Dwarf has a weak magnetic field, then the magnetic energy density is not high enough to channel the accreting material along the magnetic field lines of the WD. So the material keeps free-falling, and due to conservation of angular momentum, it forms an accretion disk around the WD and some of the material in the disk spirals down, preferentially onto the equatorial region of its surface. This class is called non-magnetic cataclysmic variables (Connon Smith, 2007).

If the White Dwarf's magnetic field is of the order of 10 MG, the magnetospheric radius is large enough to completely prevent the formation of an accretion disk, as the accreting ionized material gets captured by the magnetic field lines of the WD and moves along them. The material accelerates along the magnetic field lines, falling towards the nearest magnetic pole(s) of the WD (see Figure 1.2). As it approaches the WD's surface near the magnetic pole(s), it accelerates to the WD's escape velocity, which creates a strong shock at impact. This leads to the emission of radiation in various parts of the electromagnetic spectrum by the post-shock flow (Cropper, 1990). X-rays

primary mass   :   1.00 M$_{Sun}$ period   :   3.33 hours
secondary mass :   0.50 M$_{Sun}$ inclination   :   45.00 degrees
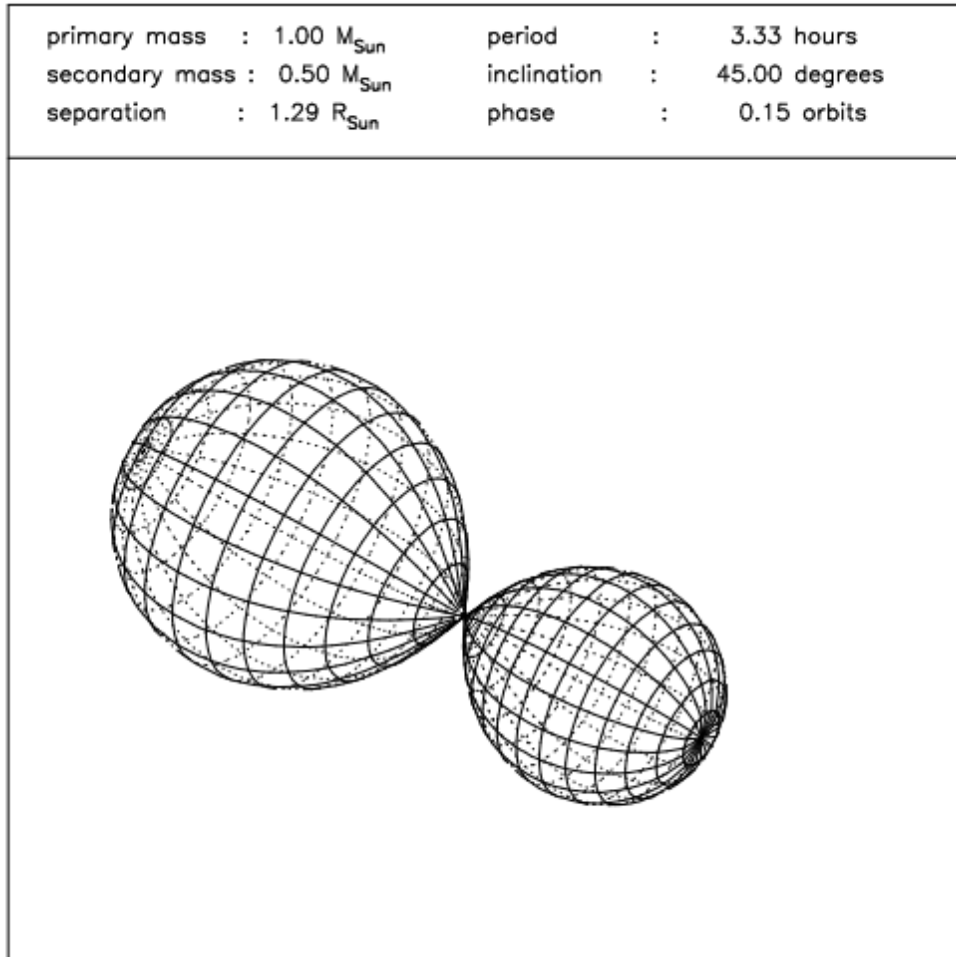separation   :   1.29 R$_{Sun}$ phase   :   0.15 orbits

Figure 1.1: An example diagram of 3 dimensional Roche lobes of the stars in a binary system, the parameters of which are shown. Notice how they are tear-shaped, and meet at the inner Lagrangian point where the forces balance (from Connon Smith, 2007). The higher mass star in the binary is called the primary, and the lower mass star is the secondary.
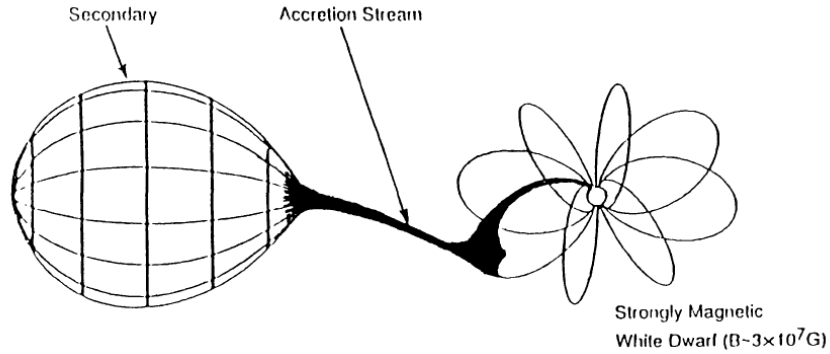
Figure 1.2: Schematic of a polar, from (Cropper, 1990). Notice the absence of an accretion disk due to the significant strength of the magnetic field of the WD, and how the accretion stream is moving towards the one magnetic that is closer to the secondary.

of varying energies are emitted. High energy (or hard, e.g, ¿ 2 keV) X-rays are emitted as Bremsstrahlung radiation due to the cooling of the charged particles in the post shock flow. Lower energy (or soft) X-rays result from part of the hard X-rays being absorbed by the WD's surface, being thermalized, then re-emitted as blackbody radiation, which peaks in the soft X-rays and far-ultraviolet (Imamura and Durisen, 1983). Near-infrared and optical emission occurs when the post-shock material spirals around the WD's magnetic field lines, forming polarized cyclotron radiation. These systems are called polars, because of their strongly polarized cyclotron emission indicating the high magnetic field strength of the WD (see Cropper, 1990, for an extensive review).

In an intermediate case between polars and non-magnetic CVs, the magnetic field of the WD is weaker than in polars (measured by their weaker observed polarization) and stronger than in non-magnetic CVs. In this case, the material does form a disk around the White Dwarf. However, this disk breaks down at the WD's magnetospheric radius, where magnetic energy density of the WD is stronger than the kinetic energy density in the inner parts of the disk. Here the material starts moving along the magnetic field lines of the WD, accelerating towards its magnetic poles. This creates a truncated disk around the WD
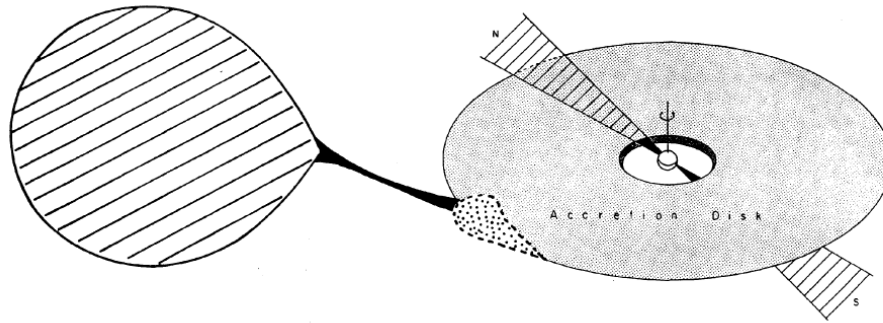
Figure 1.3: Schematic of an intermediate polar, from (Patterson, 1994). Notice the truncated accretion disk at the WD's magnetospheric radius, with two accretion streams from its inner parts moving towards the WD's magnetic poles. Also notice how radiation from the accretion regions on the WD can heat parts of the disk.
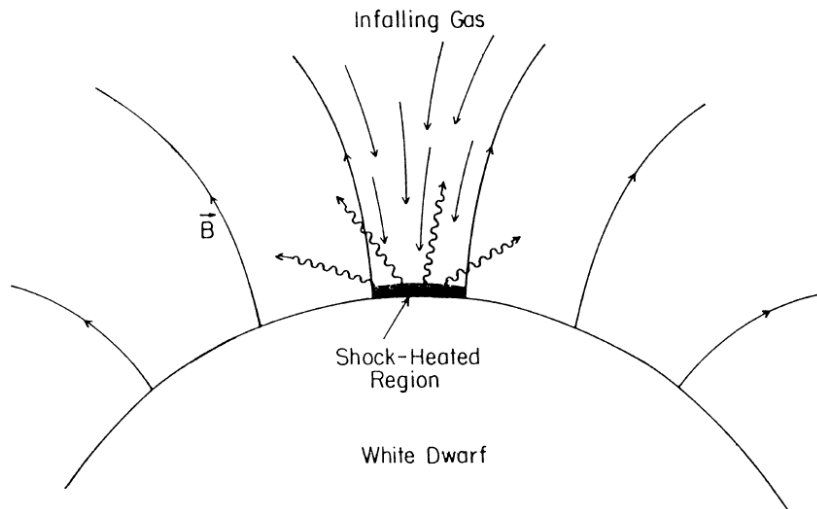
Figure 1.4: Schematic of the accretion region, see (Cropper, 1990). The hard X-rays are initially emitted isotropically, half of which goes into the WD's surface, gets thermalized and re-emitted as soft blackbody X-rays. The other half partially escapes to infinity, and partially gets scattered back into the WD. See Chapter 4 for a more in-depth discussion of this.

(see Figure 1.3). These systems are called "intermediate polars" (IPs), since they exhibit behaviours of both polars and non-magnetic CVs, namely, an accretion disk, then accretion streams that follow the magnetic field lines of the WD. (Patterson, 1994). Note, however, that there could also be intermediate polars with no accretion disk, as Wynn and King (1992) found them hard to rule out by comparing theoretical power spectra of diskless IPs compared to observations. And a diskless IP has been indeed observed: V2400 Oph (Hellier and Beardmore, 2002). The focus of my thesis will be magnetic CVs, namely, polars and intermediate polars.

1.2 Observed X-ray timing signatures in magnetic CVs

In most cases, the magnetic axis of the WD in mCVs is tilted relative to its rotational axis, so that the magnetic poles (and thus the accretion regions emitting the radiation) each occupy a small region away from the rotational poles. Therefore, the observed brightness of soft and hard X-rays emitted from an accretion region near a magnetic pole of the WD will vary with WD spin phase, depending on whether the magnetic poles rotate in and out of our line of sight, or one pole stays continuously in view. This variation pattern – and hence the shape of the soft and hard X-ray light curves – depends on the geometry of the system (which will be discussed in depth in chapter 4). This X-ray brightness modulation due to the WD spin matches the orbital period in most polars, because the strong magnetic field of the WD interacts with the companion star, slowing the WD rotation to match the orbit. Typical orbital periods in polars range from 1.3 to 3.5 hours.

While in intermediate polars, the WD's magnetic field is not strong enough to bring the spin of the WD to synchronism with the binary orbit, so we may see less direct evidence of the orbital period in their X-ray light curves. These

include: eclipses of part or all of the truncated accretion disk by the secondary, signals produced by the reflection of radiation from near the WD magnetic pole off the secondary star, and radiation from a heated spot at the disk's edge. This heating produces a signal one fewer time per binary orbit than we see from the magnetic pole directly, so it comes at the lower "orbital sideband" frequency $\omega_{repro} = \omega_{spin} - \Omega_{orb}$. Observed WD spin periods in IPs range from about half a minute to around 2 hours, and orbital periods between around 1.6 to 48 hours. (Patterson, 1994).

1.3   Asynchronism in Magnetic CVs

As mentioned above, in most known polars, the rotation of the WD is synchronous with the orbital period of the binary. In this case, the orientation of the magnetic axis of the WD will remain the same with respect to the secondary at all times, and hence the plasma stream from the secondary will accrete near the same magnetic pole(s) at all times as the WD co-rotates with the mutual orbit of the companions. (see Cropper, 1990).

However, if there is even a slight asynchronism between the WD spin period and binary orbital period (with a non-zero angle between the WD spin and magnetic axes, or a spin axis that is not perpendicular to the orbital plane in the case where the spin and magnetic axes align), the orientation of the WD's magnetic axis with respect to the secondary will keep changing, and hence, the plasma stream will periodically switch to magnetic field lines leading it to the other magnetic pole. Figure 1.5 is a simple schematic demonstrating this switch. Note that it is not to scale, and it is assuming that the accretion regions are separated by 180°. This process will be discussed in more detail in Chapter 5.

This phenomenon can be observed as a phase shift of the spin modulation in the X-ray light curves of the mCV (since the spin-modulated X-rays are

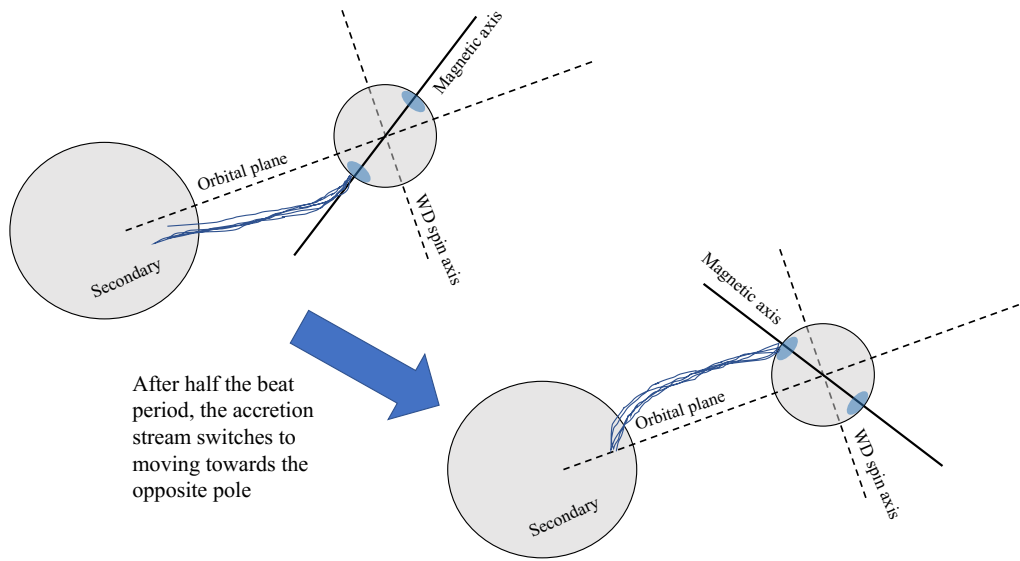Figure 1.5: Schematic of an asynchronous polar, demonstrating the switch of the accretion stream between the magnetic poles due to changes in the orientation of the WD magnetic field with respect to the secondary. Note that it assumes a separation of accretion regions of 180° and it is not to scale. For further explanation of this process and the period at which the switch occurs, see Chapter 5.

emitted by the accretion region(s)). The amount of this phase shift and the frequency at which it occurs is dependent on the angular separation of the two accretion regions on the surface of the white dwarf and the degree of asynchronism between the WD spin and binary orbital periods (see Chapter 5). However, the observability of two accretion regions near opposite magnetic poles of the WD in X-rays depends on the geometry of the system; namely, on the angle between the WD's magnetic and rotational axes, and the inclination of the system (which will be explored in Chapter 4, based on the model from (Imamura and Durisen, 1983)).

This phenomenon of the accretion stream switching between opposite poles due to asynchronism can occur in diskless intermediate polars, since their WD's magnetic field is not strong enough to synchronize its spin with the binary orbital period. It also occurs in a few polars with a slight asynchronism between the WD spin and binary orbital periods, which are called asynchronous polars (APs). A suggested reason for their asynchronism is the occurrence of a nova explosion on the WD surface. If a nova explosion happens to an initially synchronous polar, the rapid expansion of the envelope of the WD increases the moment of inertia of the WD, which initially slows down the WD's spin (due to conservation of angular momentum). Then due to a strong magnetic coupling between the secondary and the post-nova envelope, the WD spin goes back up rapidly towards re-synchronization. However, the remnants of the nova envelope start contracting, causing the WD to spin up again, towards asynchronism. This process has been observed in the confirmed asynchronous polar V1500 Cyg, and the suspected asynchronous polar V4633 Sgr. (Stockman et al., 1988; Pavlenko et al., 2018) (Lipkin and Leibowitz, 2008)

Confirmed (and two other candidate) asynchronous polars are listed in Table **??**, with 1RXS J083842.1-282723 being the most recent (see Halpern et al., 2017). One can notice from Table **??** that most of these asynchronous polars have periods ranging from ∼ 1.8 to 3.4 hours, with a spin-orbit degree of

asynchronism $\frac{P_{orb}-P_{spin}}{P_{orb}}$ of $\lesssim 2\%$ .Two mCVs, Paloma and IGR J19552+0044 were found to have degrees of asynchronism higher than in typical asynchronous polars, thus leading to the conclusion that these systems are either highly asynchronous polars, or diskless near-synchronous intermediate polars (that could be evolving towards synchronism and thus towards becoming polars) (Schwarz et al., 2007; Joshi et al., 2016; Bernardini et al., 2013; Tovmassian et al., 2017)).

Over timescales estimated from several tens to several thousands of years, APs tend to evolve towards synchronism due to angular momentum loss by the WD (Myers et al., 2017). In most APs, the WD spin period is slightly shorter than the binary orbital period, and as a result of dissipation caused by magnetic interactions between the synchronous WD and the secondary, the WD loses angular momentum and its spin period slowly decreases to match that of the binary orbit. (Campbell, 1984) So we see that by observing changes in the periodicities of asynchronous magnetic CVs over the years one can obtain observational values of synchronization timescales, and along with studying changes in their accretion geometries, these systems provide laboratories for testing the validity of magnetic theories of how such systems form and evolve.

1.4 Overview of thesis structure

In this thesis, I will be discussing the approach and results of my studies of X-ray data of the system X10 (aka W27, aka CXOGlb J002406.3-720443) in the star cluster 47 Tuc, which is believed to be an asynchronous magnetic cataclysmic variable (Heinke et al., 2005). In Chapter 2, I will show the observed X-ray light curves and spectra of X10, obtained by the Chandra X-ray Observatory, and discuss how they lead to the hypothesis that the system exhibits pole-switching behaviour of the accretion stream, possibly due to asynchronism. In Chapter 3, I will show the power spectra and least squares fitting of

System	P_{spin} mins (hrs)	P_{orb} mins (hrs)	$\frac{P_{orb}-P_{spin}}{P_{orb}}$	References
BY Cam	199.33 (3.3222)	201.26 (3.3543)	0.96%	Silber et al. (1992); Mason et al. (1998)
V 1500 Cyg	197.50 (3.2917)	201.04 (3.3507)	1.76%	Stockman et al. (1988); Pavlenko et al. (2018)
V1432 Aql	202.51 (3.3751)	201.94 (3.3656)	−0.28%	Geckeler and Staubert (1997)
RX J2115-5840	109.55 (1.8258)	110.89 (1.8482)	1.21%	Ramsay et al. (1999)
1RXS J083842.1-282723	94.8 (1.58)	98.3 (1.64)	0.037%	Halpern et al. (2017)

Table 1.1: Confirmed asynchronous polars.

the X-ray light curves indicating the spin period of the WD and highlighting the phase shifts. In Chapter 4, I will explore the geometry of the system (and hence whether or not observing it allows the viewing of two opposite poles) through a simulation of the X-ray light curves based on the model of Imamura and Durisen (1983), and compare it to observations to set rough constraints and visualize the system. In Chapter 5, I will derive a range of possible values of the orbital period of X10 and hence, a range of possible degrees of asynchronism of the system (the value of which determines the classification of the system as either a Polar or an IP) through analyzing the overall behaviour of the light curve phases and amplitudes, and discuss the complications that arise when trying to find the system's exact orbital period with the available data. Finally, Chapter 6 will tie together the conclusions.

Chapter 2

Observations and preliminary analysis

2.1 Background on globular clusters, and X10's X-ray observations

In this section, I will provide some background information on 47 Tuc and X10. First I would note that globular clusters have high rates of stellar interactions (for an overview of globular cluster dynamics, see Meylan and Heggie, 1997), which lead to an overabundance of bright low-mass X-ray binaries in globular clusters (Pooley et al., 2003), especially in the densest clusters (Clark, 1975; Jordán et al., 2004), and also to enhanced production of fainter X-ray sources, particularly cataclysmic variables (Heinke et al., 2006; Pooley and Hut, 2006).

47 Tuc is a globular cluster 4.53 kpc away, (Bogdanov et al., 2016), with an estimated total mass of order $\sim 10^6$ solar masses (Heinke et al., 2005), core radius of 0.36 arcminutes [1], and with one of the highest rates of stellar interactions (Pooley et al., 2003).

X-ray emission from 47 Tuc was first seen with the Einstein X-ray satellite,

[1]https://physwww.physics.mcmaster.ca/~harris/mwgc.dat

and suggested to be due to cataclysmic variables (Hertz and Grindlay, 1983). But Verbunt et al. (1984) argued that this emission was more likely due to LMXBs with neutron stars, in quiescence between outbursts; but at this time, neither X-ray nor optical telescopes were able to resolve the observed X-ray emission into multiple sources, or able to search for faint optical counterparts in the crowded globular cluster (for example, see Auriere et al., 1989, where an attempt was made to match X-ray data of 47 Tuc from the Einstein satellite with optical data). The Hubble Space Telescope allowed identification of several cataclysmic variables in 47 Tuc, which might be associated with the X-ray emission (for example, see Paresce et al., 1992; Shara et al., 1996) (note that in the latter reference, the optical variable V3 was identified, which was later shown to be X10's optical counterpart).

The ROSAT X-ray telescope had higher angular resolution ($\sim$2"), allowing the resolution of X-ray emission associated with the core of 47 Tuc into 4, then 9 X-ray sources (Hasinger et al., 1994; Verbunt and Hasinger, 1998). The Chandra X-ray Observatory's better sensitivity and 0.5" angular resolution allowed the resolution of 47 Tuc's X-rays into 300 sources (Grindlay et al., 2001; Heinke et al., 2005), with positions accurate enough to identify scores of optical counterparts, including cataclysmic variables, chromospherically active binaries, and millisecond radio pulsars (Edmonds et al., 2003b,a; Rivera-Sandoval et al., 2015; Rivera Sandoval et al., 2018). The brightest few sources, for which the ROSAT X# names have been retained, include three quiescent low-mass X-ray binaries with neutron stars (Heinke et al., 2003), a likely black hole low-mass X-ray binary (Miller-Jones et al., 2015; Bahramian et al., 2017), and a number of CVs, identified by optical counterparts that are very blue and highly variable (Edmonds et al., 2003b).

The most X-ray luminous of the CVs in 47 Tuc is X10. Grindlay et al. (2001) (using 72 ksec of Chandra data, taken in 2000) confidently identified it with the blue, variable star V3, and suggested a CV interpretation. They noted the

unusually soft X-ray spectrum, and suggested a 3.83 hour possible periodicity. Edmonds et al. (2003a) showed evidence from Hubble for a very blue component (dominating ultraviolet light) and a redder component, likely a main-sequence star, dominant in visible and infrared light -these can be identified with the accretion disk or WD, and companion star, of a CV, respectively. Edmonds et al. (2003b) noted a possible periodicity at 3.7 hours in the optical data, though several other peaks in their power spectrum reached similar power. Heinke et al. (2005) used a further 300 ksec of Chandra data (from 2002) to argue for a 4.67 hour strong sinusoidal periodicity, and fit the X-ray spectrum with a very soft blackbody (53 ± 4 eV) plus two thermal plasma (MEKAL, (Liedahl et al., 1995)) components at 0.39 ± 0.03 keV and > 14 keV. Heinke et al. (2005) argued from the spectrum and periodicity that X10 is likely a polar.

2.2   Data processing for X10

I have examined thirteen Chandra observations of the magnetic cataclysmic variable X10 in 47 Tuc. The available observations are from 2002, 2005, 2014 and 2015, the details of which are listed in Table 2.1. The 2002 data were taken with Chandra's ACIS-S detector, providing good energy resolution (Garmire et al., 2003), over a 2-week period. The 2005 data are part of 800 ks of data taken over a couple months with the HRC-S detector, which provides higher time resolution (less than a millisecond), but with very poor energy resolution and lower sensitivity (Murray et al., 2000). The 2014 data were taken with ACIS-S, however the sensitivity of this detector to soft X-rays has degraded significantly between 2002 and 2014 due to the buildup of a contaminant on the detector (Plucinsky et al., 2016). The observations in Table 2.1 are the ones which give the best signal -there are another 11 HRC-S observations from 2005, ACIS-I observations from 2000, and two 2014 ACIS-S observation that

ObsID	Interval	Detector	Observation date
2735	67 ks	ACIS-S	2002-09-29
2736	67 ks	ACIS-S	2002-09-30
2737	67 ks	ACIS-S	2002-10-02
2738	70 ks	ACIS-S	2002-10-11
5542	52 ks	HRC-S	2005-12-19
5543	54 ks	HRC-S	2005-12-20
5544	52 ks	HRC-S	2005-12-21
5545	54 ks	HRC-S	2005-12-23
15747	57 ks	ACIS-S	2014-09-09
15748	19 ks	ACIS-S	2014-10-02
16527	45 ks	ACIS-S	2014-09-05
16528	45ks	ACIS-S	2015-02-02
16529	27 ks	ACIS-S	2014-09-21

Table 2.1: Observations of 47 Tuc which I used to study X10.

all provide an inferior signal from X10.

Using the ds9 software, I created a source region file for each observation with a radius of 1.7 arcseconds, located at RA=0:24:06.374, DEC=-72:04:43.00 (Heinke et al., 2005). Background region files were created as well, of radius 9 arc seconds and a centre at RA=0:24:13.836, DEC=-72:04:13.18. I was able to select a standard background for all observations since there were no flares or periodic variabilities detected in the light curves of the backgrounds. Plus, there were no significant differences between the source light curves and the background-subtracted ones. Then using Chandra's CIAO software [2], I applied barycentric corrections to each observation by correcting for the good time intervals (GTIs) and correcting the aspect solution files, using the axbary command. Afterwards, I merged the barycentered data files for each year, and then obtained the background subtracted light curves seen in Figure 2.1 from them using the dmextract command in CIAO.

---

[2]http://cxc.harvard.edu/ciao/manuals.html

2.3   A first look at the X-ray light curves

Figure 2.1 shows the resulting background-subtracted X-ray light curves of X10 for all the observations listed in Table 2.1, binned at 1000 seconds. Where the y-axis "CR" stands for the count rate: the total number of counts per bin length, and where the error in the count rate is Gaussian [3], and the ACIS-S light curves are extracted at energies between 0.2 and 10 keV. The observed X-ray light curves are modulated at the WD's spin period, since the X-rays are emitted by the post-shock flow at the accretion region near a magnetic pole. So the light curve maxima and minima occur as the accretion region moves in and out of our view (respectively) as the WD spins (Cropper, 1990). One can see large (typically $\sim$100%) amplitude variations in the light curves. In some instances, the amplitude seems to change suddenly (as seen in obsID 2735), and in other instances, it changes more gradually with a smooth pattern (as seen in obsID 2736 and obsID 5543). In this Figure, the tick marks are periodic, repeating every 4.185 hours, beginning from the first peak in the first 2002 observation (obsID 2735). The reason for choosing the period of 4.185 hours is that it is the derived spin period of the WD from power spectrum analysis, and sinusoidal least squares fit to the observed light curves. A full discussion of this will follow in Chapter 3.

One can see in Figure 2.1, for example, that these tick-marks correspond to the maxima of the first two cycles in obsID 2735, and afterwards in this observation, about halfway between consecutive tick-marks, additional maxima start appearing and increasing in amplitude. And in the next observation (obsID 2736), the same tick-marks (repeating every 4.185 hours, starting from the same point mentioned above) now correspond to the minima of the cycles. Treating the signals as sinusoids, this transition of the same periodic tick-marks corresponding to maxima and then to minima, is a shift in the sinusoid's phase.

---

[3]http://cxc.harvard.edu/ciao/ahelp/dmextract.html

Interpreting this sinusoidal pattern as a result of emission from an accretion region near the WD's magnetic pole coming in and out of view as the WD spins, then a shift in this sinusoid's phase by about half a cycle, can be interpreted as a result of the accretion stream switching its trajectory towards the opposite WD magnetic pole. Thus resulting in a bright accretion region located near the opposite magnetic pole of the WD, coming in and out of view as the WD spins. And when both phases appear in the same observation (as in obsID 2735), the two accretion regions near the opposite magnetic poles are probably active at the same time, as when the first comes out of view, the opposite one comes into view. This can also be seen in obsID 15747.

2.4 The X-ray spectra and their fits

I also looked at the X-ray spectrum of the merged and barycentre-corrected set of 2002 (obsIDs 2735, 2736, 2737 and 2738) and 2014 (obsIDs 15747, 15748, 16527, 16528 and 16529) Chandra ACIS-S observations. Using the HEASOFT XSPEC software [4], I have fitted both spectra from 0.3 KeV to 11 KeV with a fixed neutral gas column of $N_H = 3.5000 \times 10^{20}$, blackbody (bbodyrad in XSPEC), vmekal and mekal components (emission models for hot diffuse gas that include Bremsstrahlung continuum and line emission, where I set fixed sub-solar element abundances). The fit parameters are displayed in Table 2.2 and the fitted spectra are shown in Figure 2.2. The reason for these choices for the fit models is the soft X-rays resulting from the shock-generated hard X-rays getting absorbed by the WD's surface, thermalized and re-emitted as blackbody radiation from the accretion region (see discussion in Chapter 1). And the vmekal and mekal components fit the hard X-rays with Bremsstrahlung models along with continuum line emission (Liedahl et al., 1995). The resulting spectral fit parameters are consistent with those found for X10 in Heinke et al.

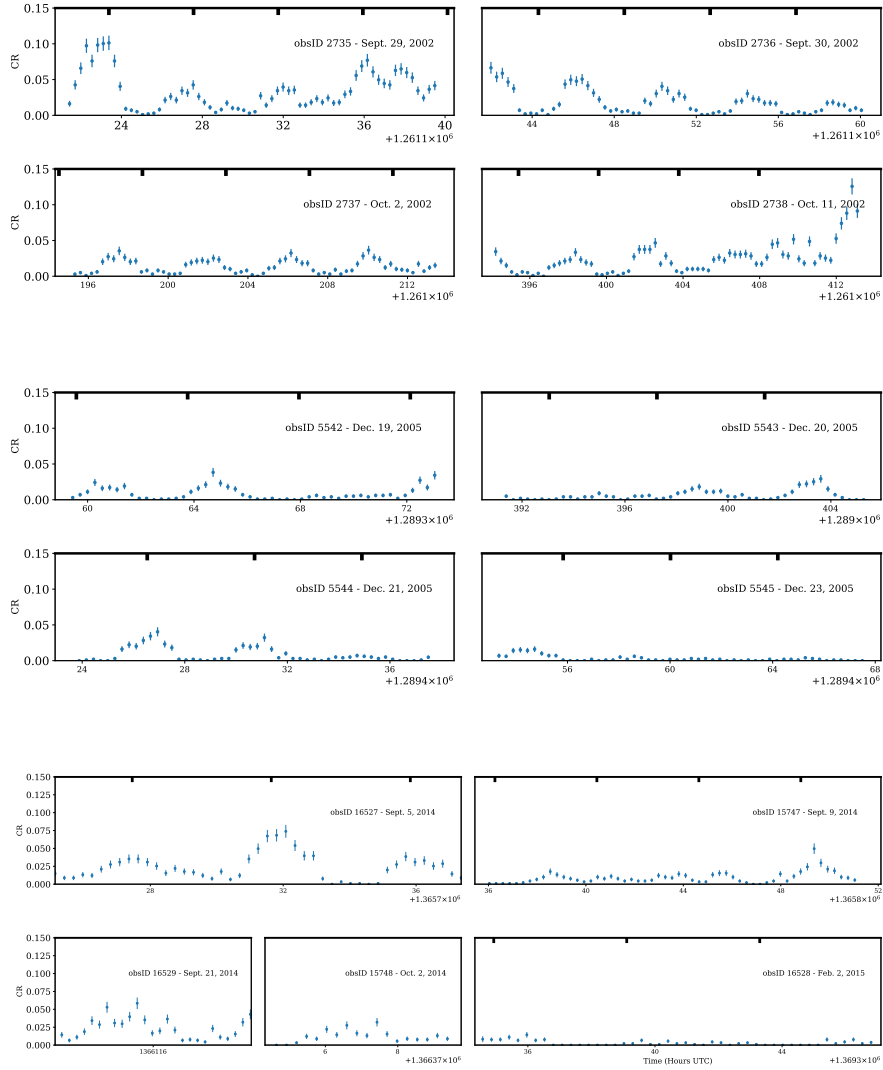[4]https://heasarc.gsfc.nasa.gov/docs/xanadu/xspec/

Figure 2.1: Observed X-ray light curves of X10

(2005), and with expectations for a polar ((see Kuulkers et al., 2006). For examples of X-ray spectra of polars, see Ramsay et al. (2004); Halpern et al. (2017)). The fact that the X-ray spectrum hasn't changed significantly implies that the accretion region on the WD (from which the X-rays are emitted) has not gone through significant changes between 2002 and 2014/2015, unless there were some short-term changes experienced there sometime in-between the available observations.

Table 2.2: Spectral fit parameters

| Parameter	Merged 2002 data	Merged 2014 data
N_H	3.5000×10^{20}	3.5000×10^{20}
kT_{bb}	49 ± 2 eV	31 ± 2 eV
$bbodyradnorm$	$1.6 \times 10^{+04} \pm 5.0 \times 10^{+03}$	$1.3 \times 10^{+07} \pm 1.1 \times 10^{+07}$
kT_{vmek}	389 ± 25 eV	326 ± 24 eV
$vmekalnorm$	$38 \times 10^{-06} \pm 2 \times 10^{-06}$	$70 \times 10^{-06} \pm 6 \times 10^{-06}$
kT_{mek}	23 ± 10 keV	$43.7891\pm > 13.5$ keV
$mekalnorm$	$38 \times 10^{-06} \pm 2 \times 10^{-06}$	$48 \times 10^{-06} \pm 9 \times 10^{-06}$
$F_{0.5keV-10keV}$	8.880×10^{-14} erg cm^{-2} s^{-1}	1.1927×10^{-13} erg cm^{-2} s^{-1}
$F_{0.5keV-2keV}$	4.0074×10^{-14} erg cm^{-2} s^{-1}	5.8097×10^{-14} erg cm^{-2} s^{-1}
$chi^2/d.o.f$	0.9761	0.811
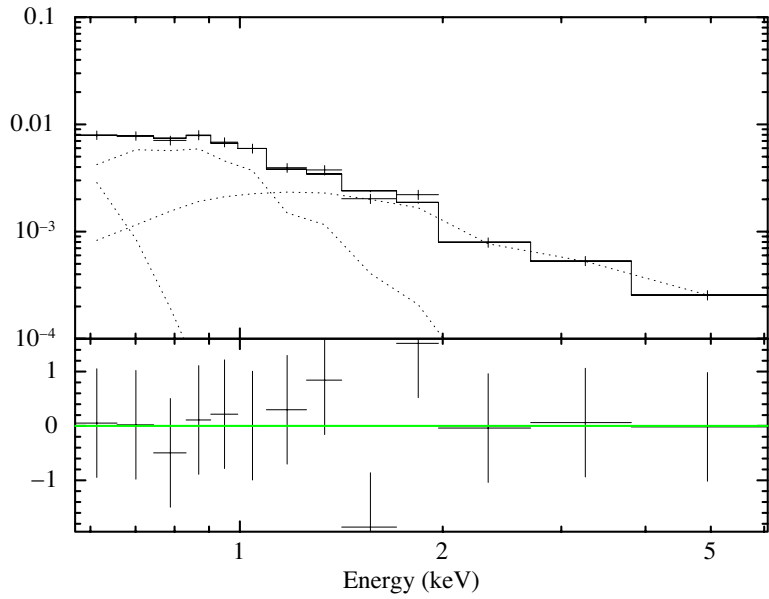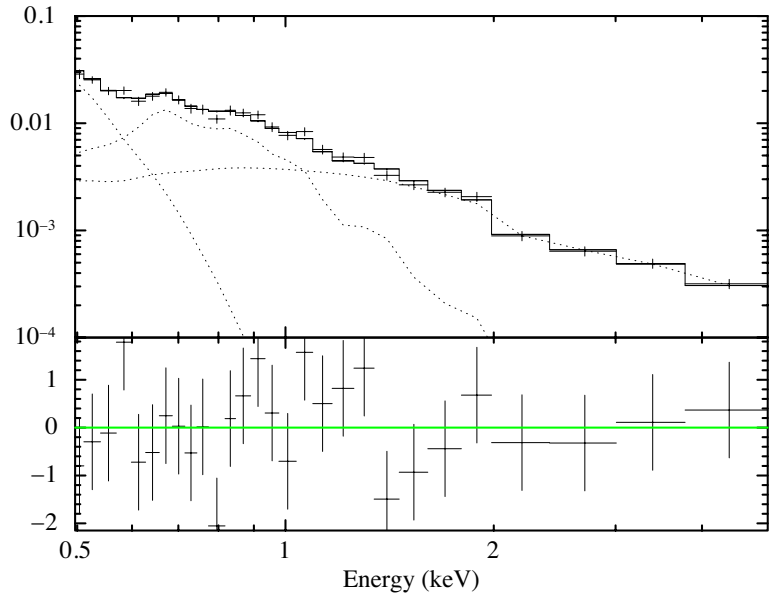
Figure 2.2: Fitted X-ray spectra of X10 from 2002 (upper) and 2014/2015 (lower). The upper panels give the flux (the data points are crosses and the model is the straight line) in photons s^{-1} cm^{-2} keV^{-1}, and the lower panels give the residuals between the data and the model in units of the error in the data.

Chapter 3

Exploring the light curve spin modulation and phase shifts

In this Chapter, I will discuss my analysis of the X-ray light curves of X10 to obtain its spin period through its power spectrum and least squares fits to the data. I will also discuss the observed phase shifts in the modulation and explore the hypothesis that the opposite phases correspond to two different accretion regions near opposite magnetic poles on the WD.

3.1   The X-ray power spectra of X10

I used the astropy.stats.lombscargle package (VanderPlas et al., 2012) to create power spectra for X10, using light curves of the four long 2002 Chandra ACIS-S observations merged together, the merged light curve of two adjacent long ACIS-S observations, the merged 2005 HRC-S Chandra observations, and several single observations. These power spectra are shown in Fig. 3.1 and Fig. 3.2. To estimate the errors in the peaks of the power spectra, I used the astropy.stats.bootstrap package [1]. I used this package to perform bootstrap resampling of arrays that are $\frac{2}{3}$ the length of the original ones, to produce 10,000

---

[1]http://docs.astropy.org/en/stable/api/astropy.stats.bootstrap.html

23

sample power spectra, the peaks of which form a distribution. I adapted the standard deviation of the peak distribution as the confidence interval for the peak of the full power spectrum. One can notice two main patterns in these power spectra: (1) The power spectra of separate observations that show no phase shifts have a single peak at the spin frequency of the WD (within error limits), as in Figures 3.1(c), 3.2(e) and 3.2(f). (2) The power spectra of merged observations show many peaks due to the presence of phase shifts and amplitude variations, and specifically show a pronounced double-peak pattern around the true spin frequency, as in Figures 3.1(a), 3.1(b) and 3.2(d). A similar behaviour has been observed in the power spectra of the asynchronous polar 1RXS J083842.1-282723 with pole-switching accretion (see Figure 8 of (Halpern et al., 2017)). For example, the highest peaks in the power spectrum of the merged 2005 data are at $7.15 \pm 4.33 \times 10^{-5}$ s^{-1} and $5.91 \pm 4.70 \times 10^{-5}$ s^{-1} (note the huge errors!), corresponding to modulations of 3.89 ± 2.56 and 4.70 ± 3.44 hours. These modulations roughly agree within error with the 3.7 hour periodicity in the optical data suggested by Edmonds et al. (2003b), and the 4.67 hour periodicity argued by Heinke et al. (2005), respectively.

In Fig. 3.1(c) from the third 2002 observation (obsID 2737), the observed peak frequency is $6.57 \pm 0.13 \times 10^{-5}$ s^{-1}. In the third 2005 observation (obsID 5544), the peak is consistent (with a much bigger error) at $6.54 \pm 1.62 \times 10^{-5}$ s^{-1}. Finally, the peak is at $6.52 \pm 0.15 \times 10^{-5}$ from ObsID 15747 taken in 2014, which is consistent within the errors with the other two frequencies.

These frequencies correspond to modulations of 4.23 ± 0.08, 4.25 ± 1.05 and 4.26 ± 0.10 hours, respectively. Hence, from the power spectra analysis alone, I cannot tell if the spin period has changed between 2002, 2005, and 2014. Due to the phase shifts in the modulation, and due to the apparently unpredictable variations in the modulation amplitudes in the light curves of the available data, trying to obtain informative power spectra with clear, unique peaks from the merged observations is almost impossible. Some observations are either

too short, and/or contain both phases together, which creates unreliable power spectra. Figs. 3.1 and 3.2 show the power spectra of the observations that show the cleanest and clearest pulsations in our data.

3.2 Least-squares fitting of the X-ray light curves of X10

Informed by the period corresponding to the peak in the power spectra as an initial guess, I fit the light curves using the least-squares fitting algorithm from scipy.optimize on python. The functional form chosen to find a best fit is:

$$CR(t) = A \sin{(\omega t - \phi)} + B \qquad (3.1)$$

Where A is the amplitude, ω is the WD spin angular frequency, ϕ is the phase, and B is the vertical offset. In these fits, I am not allowing the amplitude to be an explicitly defined function of time (as this would be determined by an amplitude envelope function related to the system's orbital period - which is unknown; see Chapter 5 for a full discussion). However, I let A be a free parameter that varies between different cycles, with an initial guess based on the observed count rate in the cycle, since the light curves show amplitude variations. The vertical offset was needed since the sinusoids for the light curve cannot have negative values, and was set to be a free parameter as well. The phase ϕ, also a free parameter, because I needed to account for, and measure, the light curve phase shifts that were discussed in Chapter 2 (see Figure 1.5 in Chapter 2 and its discussion). Figure 3.3 shows the least-squares fitted light curves, and Table 3.1 shows the fitting parameters. Attempting to fit the light curves, I decided to start with the third 2002 observation (obsID 2737), because it appears to have the longest "well-behaved" light curve; with a single phase and with near-constant amplitude (see Figure 3.3). I let the spin

angular frequency ω for this observation to be a free parameter, with its initial guess being the value from the peak of the corresponding power spectrum: $\omega_{guess} = 2\pi \times 6.57 \times 10^{-5} = 4.13 \times 10^{-04}$ rad s^{-1}. This guess made sense to me since the Lomb-Scargle power spectra themselves are based on sinusoidal models of the data (VanderPlas et al., 2012), and the power spectrum peak for this observation has the smallest error compared to the other observations that show a single peak (see Fig. 3.1(c) versus Figs. 3.2(e) and (f)). The resulting spin angular frequency from the least squares fit to obsID 2737 is $\omega = 4.171 \times 10^{-04} \pm 0.037 \times 10^{-04}$, which corresponds to a spin period of $P_{spin} = 4.185 \pm 0.038$ hours. Then I found that I had to fit most cycles in the other observations individually due to various complications in the light curves. E.g., in the case of varying amplitudes within the same observation, and/or when there are two opposite phases both appearing within the same observation (suggesting material falling onto both accretion regions at the same time), as seen in the first 2002 and 2014 observations. With the amplitude, phase and vertical offset being free parameters for these other observations where I had to separately fit the cycles, the range of possible spin periods that produced minimal chi-squared turned out to be quite large and produced large errors in the resulting fits when the spin angular frequency was set to be a free parameter (even though the initial guess for ω was the same one used for obsID 2737). For this reason, and the fact that the spin period for an asynchronous mCV does not change in the time scale covered in the observations being examined (Myers et al., 2017), I decided to fix the spin angular frequency when fitting the rest of the observations, adapting the value obtained from the least squares fit of obsID 2737, namely, $\omega = 4.171 \times 10^{-04} \pm 0.037 \times 10^{-04}$. This gave consistently good results in fitting all the data, and reduced the fit errors encountered when ω was set as a free parameter.

Note, however, that the errors in the phase ϕ are still large, especially for the phase shifts that appear as partial cycles in observations with both opposite

phases indicated by the tick-marks (like in obsID 2735 and obsID 15747, which is expected because they form a fraction of a sinusoidal cycle). And also in some cases where an observation does not seem to exactly correspond to one phase indicated by the tick-marks, nor its opposite (like obsIDs 2737, 2738 and 5542, where the tick-marks do not exactly correspond to a cycle maximum nor a minimum, as opposed to obsIDs 2736 and 5544 for e.g., where their minima and maxima clearly correspond to the tick-marks, respectively). There seem to be smaller shifts in the phases other than the one that's clearly defined by the tick-marks, increasing the errors in the fits.

Generally, in the 2002 and 2005 observations, the major phase difference lies between 150 and 170 degrees, and between 160 and 180 degrees in the 2014 and 2015 observations. The observed smaller shifts in the phases (that cause the minima and maxima of some observations not to exactly match the tick marks, as mentioned above) could be attributed to physical movement of the accretion regions on the WD surface. This is a phenomenon that has been also observed in asynchronous CVs such as V1500 Cyg (see Pavlenko et al., 2018). For a polar (or a diskless intermediate polar), the X-ray emission is coming from the accretion region near the magnetic pole. So the emission changing phase by an amount as large as $\sim 170°$ implies that the plasma stream coming from the Roche-lobe-filling secondary has switched to accreting towards the opposite magnetic pole. And both phases being present together implies that both poles are accreting (as in obsIDs 2735 and 15747). Further discussion of this will follow in the next section.
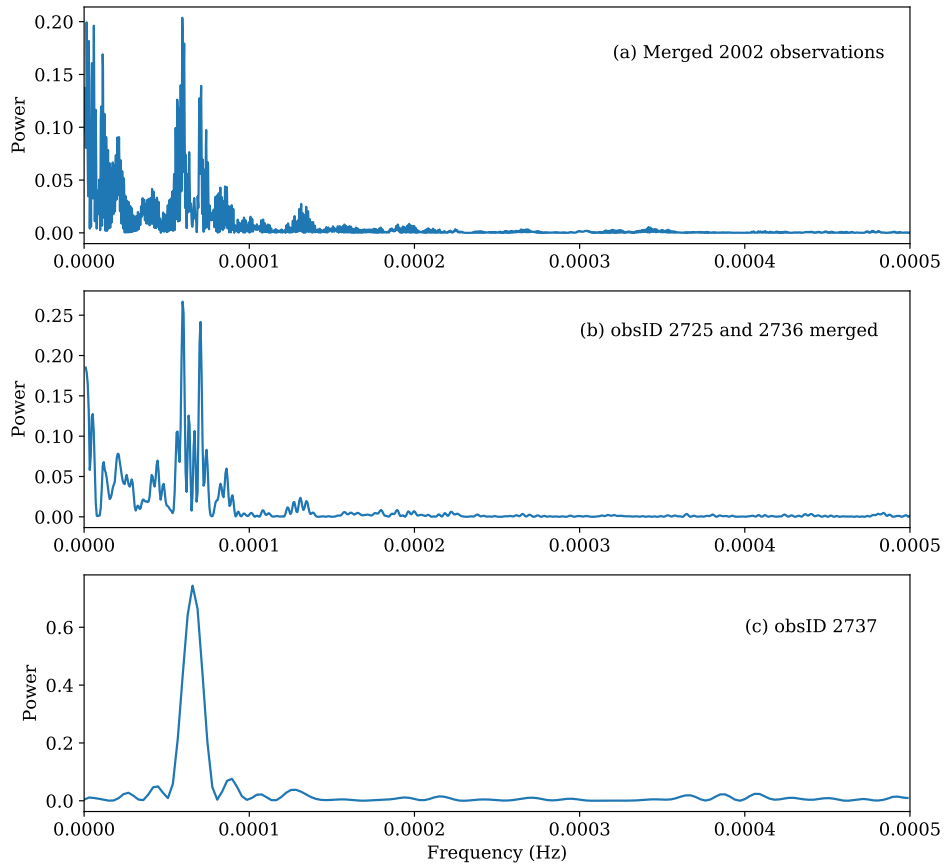
Figure 3.1: X-ray power spectra of the combined second and third 2002 observations, the second 2002 observation alone, and the third 2005 observation, respectively from top to bottom.
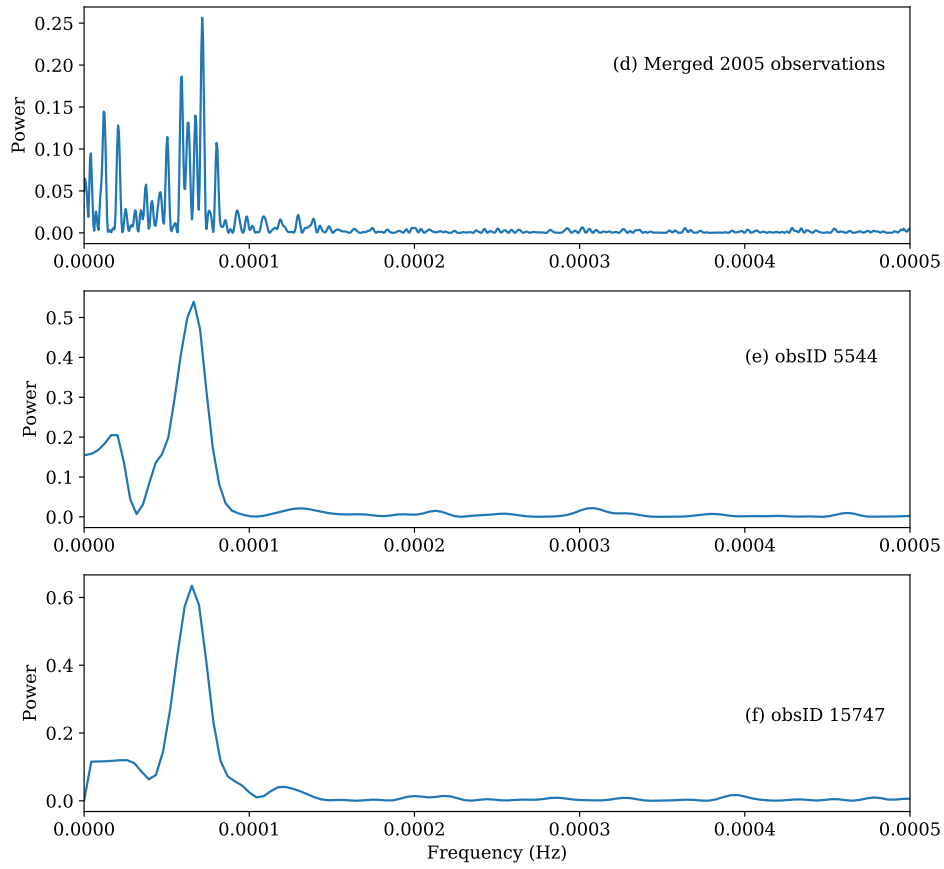
Figure 3.2: X-ray power spectra of the combined 2005 observations, obsID 5544 from 2005 alone, and obsID 15747 from 2014 alone, from top to bottom respectively.
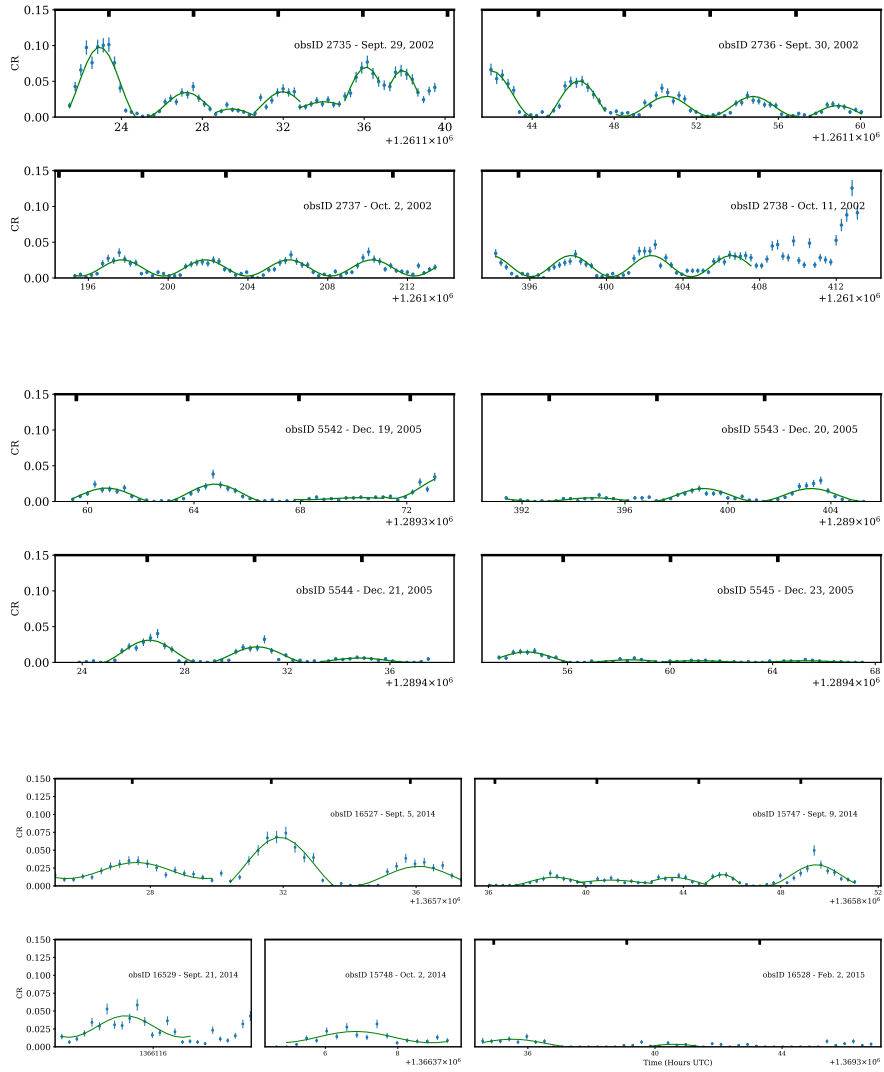
Figure 3.3: Sinusoidal fits to each observation, or parts thereof, of X10 light curves, using least squares fitting.

Table 3.1: Lightcurve least squares fit parameters.

Observation	Amplitude (A) Counts / second	ϕ radians	Offset (B) Counts / seconds
2735	$5.23 \times 10^{-02} \pm 0.51 \times 10^{-02}$	2.56 ± 0.15	$4.58 \times 10^{-02} \pm 0.51 \times 10^{-02}$
	$1.77 \times 10^{-02} \pm 0.24 \times 10^{-02}$	2.70 ± 0.12	$1.68 \times 10^{-02} \pm 0.16 \times 10^{-02}$
	$8.1 \times 10^{-03} \pm 3.8 \times 10^{-03}$	$-2.2 \times 10^{-01} \pm 2.5 \times 10^{-01}$	$3.3 \times 10^{-03} \pm 2.7 \times 10^{-03}$
	$1.94 \times 10^{-02} \pm 0.64 \times 10^{-02}$	3.58 ± 0.21	$1.61 \times 10^{-02} \pm 0.44 \times 10^{-02}$
	$6.8 \times 10^{-03} \pm 2.9 \times 10^{-03}$	$3.6 \times 10^{-01} \pm 2.3 \times 10^{-01}$	$1.46 \times 10^{-02} \pm 0.21 \times 10^{-02}$
	$4.68 \times 10^{-02} \pm 0.94 \times 10^{-02}$	3.49 ± 0.10	$2.31 \times 10^{-02} \pm 0.72 \times 10^{-02}$
	$5.21 \times 10^{-02} \pm 0.65 \times 10^{-02}$	$-1.11 \times 10^{-01} \pm 0.43 \times 10^{-01}$	$1.33 \times 10^{-02} \pm 0.52 \times 10^{-02}$
2736	$3.28 \times 10^{-02} \pm 0.31 \times 10^{-02}$	$-2.0 \times 10^{-01} \pm 1.8 \times 10^{-01}$	$3.20 \times 10^{-02} \pm 0.38 \times 10^{-02}$
	$3.15 \times 10^{-02} \pm 0.27 \times 10^{-02}$	$-8.3 \times 10^{-2} \pm 5.9 \times 10^{-02}$	$1.92 \times 10^{-02} \pm 0.17 \times 10^{-02}$
	$1.39 \times 10^{-02} \pm 0.12 \times 10^{-02}$	$1.04 \times 10^{-01} \pm 0.93 \times 10^{-01}$	$1.5005 \times 10^{-02} \pm 0.089 \times 10^{-02}$
	$1.00 \times 10^{-02} \pm 0.21 \times 10^{-02}$	$1.1 \times 10^{-01} \pm 1.3 \times 10^{-01}$	$6.1 \times 10^{-03} \pm 1.3 \times 10^{-03}$
2737	$1.15 \times 10^{-02} \pm 0.31 \times 10^{-02}$	1.1 ± 1.9	$1.403 \times 10^{-02} \pm 0.057 \times 10^{-02}$
2738	$1.49 \times 10^{-02} \pm 0.13 \times 10^{-02}$	1.103 ± 0.087	$1.658 \times 10^{-02} \pm 0.093 \times 10^{-02}$
5542	$1.10 \times 10^{-02} \pm 0.18 \times 10^{-02}$	$8.8 \times 10^{-01} \pm 1.4 \times 10^{-01}$	$7.8 \times 10^{-03} \pm 1.2 \times 10^{-03}$
	$1.32 \times 10^{-02} \pm 0.17 \times 10^{-02}$	$7.1 \times 10^{-01} \pm 1.3 \times 10^{-01}$	$1.12 \times 10^{-02} \pm 0.12 \times 10^{-02}$
	$1.40 \times 10^{-03} \pm 0.70 \times 10^{-03}$	2.67 ± 0.57	$3.97 \times 10^{-03} \pm 0.53 \times 10^{-03}$
	$1.60 \times 10^{-02} \pm 0.44 \times 10^{-02}$	1.34 ± 0.32	$2.01 \times 10^{-02} \pm 0.42 \times 10^{-02}$
5543	$2.63 \times 10^{-03} \pm 0.65 \times 10^{-03}$	1.73 ± 0.22	$2.60 \times 10^{-03} \pm 0.439 \times 10^{-03}$
	$9.2 \times 10^{-03} \pm 1.0 \times 10^{-03}$	1.89 ± 0.12	$8.96 \times 10^{-03} \pm 0.75 \times 10^{-03}$
5544	$1.68 \times 10^{-02} \pm 0.16 \times 10^{-02}$	$-7.1 \times 10^{-01} \pm 1.0 \times 10^{-01}$	$1.45 \times 10^{-02} \pm 0.12 \times 10^{-02}$
	$1.16 \times 10^{-02} \pm 0.19 \times 10^{-02}$	$-6.7 \times 10^{-01} \pm 1.6 \times 10^{-01}$	$1.03 \times 10^{-02} \pm 0.13 \times 10^{-02}$
	$3.13 \times 10^{-03} \pm 0.37 \times 10^{-03}$	$-9.6 \times 10^{-01} \pm 1.2 \times 10^{-01}$	$3.01 \times 10^{-03} \pm 0.26 \times 10^{-03}$
5545	$8.06 \times 10^{-03} \pm 0.87 \times 10^{-03}$	3.33 ± 0.10	$6.62 \times 10^{-03} \pm 0.61 \times 10^{-03}$
	$2.10 \times 10^{-03} \pm 0.88 \times 10^{-03}$	3.10 ± 0.36	$1.53 \times 10^{-03} \pm 0.60 \times 10^{-03}$
	$1.15 \times 10^{-03} \pm 0.22 \times 10^{-03}$	$7.4 \times 10^{-01} \pm 1.9 \times 10^{-01}$	$1.18 \times 10^{-03} \pm 0.16 \times 10^{-03}$
15747	$6.41 \times 10^{-03} \pm 0.79 \times 10^{-03}$	2.55 ± 0.12	$5.72 \times 10^{-03} \pm 0.56 \times 10^{-03}$
	$2.5 \times 10^{-03} \pm 1.0 \times 10^{-03}$	$-2.8 \times 10^{-01} \pm 3.2 \times 10^{-01}$	$5.67 \times 10^{-03} \pm 0.64 \times 10^{-03}$
	$7.0 \times 10^{-03} \pm 2.1 \times 10^{-03}$	3.59 ± 0.19	$4.9 \times 10^{-03} \pm 1.4 \times 10^{-03}$
	$2.45 \times 10^{-02} \pm 0.29 \times 10^{-02}$	$3.46 \times 10^{-01} \pm 0.37 \times 10^{-01}$	$-8.4 \times 10^{-03} \pm 2.3 \times 10^{-03}$
	$1.49 \times 10^{-02} \pm 0.28 \times 10^{-02}$	$-1.7 \times 10^{-01} \pm 1.8 \times 10^{-01}$	$1.47 \times 10^{-02} \pm 0.20 \times 10^{-02}$
15748	$8.0 \times 10^{-03} \pm 2.8 \times 10^{-03}$	$-1.6 \times 10^{-02} \pm 18 \times 10^{-02}$	$1.36 \times 10^{-02} \pm 0.20 \times 10^{-02}$
16527	$1.13 \times 10^{-02} \pm 0.11 \times 10^{-02}$	$-9.3 \times 10^{-01} \pm 1.1 \times 10^{-01}$	$2.149 \times 10^{-02} \pm 0.086 \times 10^{-02}$
	$3.88 \times 10^{-02} \pm 0.29 \times 10^{-02}$	$-7.32 \times 10^{-01} \pm 0.65 \times 10^{-01}$	$2.94 \times 10^{-02} \pm 0.12 \times 10^{-02}$
	$1.41 \times 10^{-02} \pm 0.33 \times 10^{-02}$	$-7.5 \times 10^{-01} \pm 2.4 \times 10^{-01}$	$1.33 \times 10^{-02} \pm 0.25 \times 10^{-02}$
16528	$1.51 \times 10^{-02} \pm 0.34 \times 10^{-02}$	2.67 ± 0.25	$2.84 \times 10^{-02} \pm 0.26 \times 10^{-02}$
16529	$5.7 \times 10^{-03} \pm 1.4 \times 10^{-03}$	$3 \times 10^{-02} \pm 24 \times 10^{-02}$	$4.9 \times 10^{-03} \pm 1.0 \times 10^{-03}$
	$4.8 \times 10^{-03} \pm 2.1 \times 10^{-03}$	1.40 ± 0.18	$-1.2 \times 10^{-03} \pm 1.6 \times 10^{-03}$

Chapter 4

Exploring the geometry of X10

In this Chapter, I will be using the model from Imamura and Durisen (1983) to simulate soft and hard X-ray light curves of X10 in various geometries. I then compare the simulated light curves with the observed light curves, to try to set rough constraints on the system's geometry -namely, the angle between our line of sight and the binary's orbital axis, and that between the WD's spin and magnetic axes. My goal is to check whether the constraints on the system geometry from pulse shape modelling are consistent with the visibility of two different accretion regions near opposite magnetic poles. If so, this would be evidence in favour of the proposition that the phase shifts in the modulation are resulting from the accretion stream switching between opposite poles.

4.1 Understanding the X-ray emission from the accretion region

In Imamura and Durisen (1983), it is assumed that the WD has a dipolar magnetic field, with a steady accretion flow from the secondary that is fully ionized and symmetric about the WD's magnetic axis, free-falling supersonically towards a WD magnetic pole and forming a shock near the surface. The accreting

material settles subsonically near the pole as a physically and optically thin post-shock flow. This shock-heated plasma will emit Bremsstrahlung radiation (hard X-rays) isotropically. At this location near the WD surface, half of this radiation will be directed outwards through the pre-shock flow, and the other half will be directed inwards towards the WD surface. The hard X-rays emitted towards the WD surface may either be absorbed by the WD surface, thermalized and re-emitted as soft blackbody X-rays, or be scattered outward into the pre-shock flow. Depending on the optical depth in the pre-shock flow, the hard X-rays that are emitted and scattered outwards will either get back-scattered towards the WD (where, again, they either get absorbed and re-emitted as soft blackbody X-rays or scattered back) or escape to infinity, thus forming the hard component of the CV's X-ray spectrum.

The optical depth of the pre-shock flow in the directions perpendicular $\tau_\perp$ and parallel $\tau_\parallel$ to the WD magnetic field (which are parallel and perpendicular to the WD surface, respectively) will affect how we see the X-rays at effectively infinite distances. According to Imamura and Durisen (1983), these relate to the fraction of the surface area of the WD occupied by the accretion region f;

$$\frac{\tau_\perp}{\tau_\parallel} = 0.95(\frac{f}{10^{-1}})^{0.5} \tag{4.1}$$

Therefore, for very small accretion regions where $f << 10^{-1}$, the optical depth in the direction perpendicular to the WD's magnetic field lines will be much smaller than that in the direction parallel to them. This will therefore cause more X-ray radiation to escape in the direction perpendicular to the WD's magnetic field lines, forming a 3-dimensional funnel shape around the accretion region. In other words, this causes the X-ray flux from the accretion region to be angle-dependent. Figure 4.1shows a rough schematic of funnelled X-ray emission around the accretion region (I edited the figure from (Cropper, 1990) to clearly show $\tau_\perp$ and $\tau_\parallel$, and how funnelled emission roughly looks like).
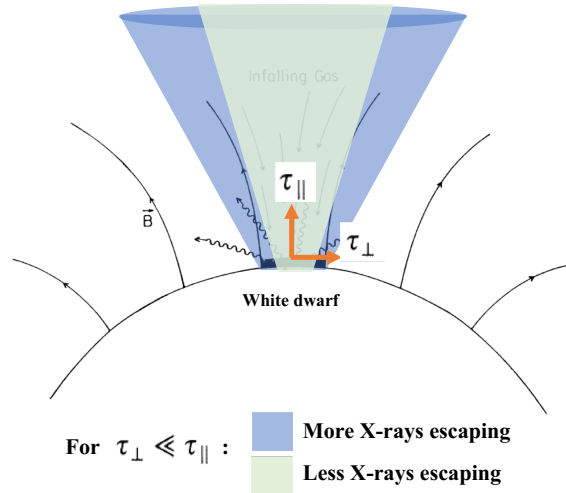
Figure 4.1: An edited schematic of the one in Cropper (1990) showing the rough shape of funnelled X-ray emission above the accretion region by a magnetic pole in a magnetic CV. Where $\tau_\perp$ and $\tau_\parallel$ are the optical depths of the pre-shock flow in the directions parallel and perpendicular to the WD magnetic field, respectively.

Imamura and Durisen computed this angular dependence for the soft black-body and hard Bremsstrahlung X-ray emission from the accretion region, dividing the accretion region into small area increments. They integrated the hydro-dynamic equations for the emission region plasma to obtain the un-degraded Bremsstrahlung spectrum, and then passing it through the pre-shock flow using Monte Carlo computations to calculate the scattering and absorption. (For more details on this computation, see Imamura and Durisen, 1983).

The results of this computation for an X-ray accretion luminosity of $L_{acc} = 5 \times 10^{34}$ ergs s^{-1} are shown in Figure 4.3, for two different values of the fraction of the WD surface area that the accretion region occupies (namely, for $f = 10^{-2}$ and $f = 10^{-4}$). In this Figure, the x-axis is $\mu = \cos(\gamma)$, with γ being the angle between the WD's magnetic axis and the line of sight (Fig. 4.2 shows these angles). Thus, when $\mu = 0.0$, then $\gamma = 90$ degrees (that is, the WD's magnetic axis is perpendicular to the line of sight), and when $\mu = 1.0$, then $\gamma = 0$

degrees (the WD's magnetic axis is parallel to the line of sight). The y-axis is the normalized flux of photons escaping in the direction of our line of sight $\mathcal{L}(\cos\gamma)$. This result depends on the ratio $\frac{L_{acc}}{f} \equiv L_f$, the X-ray accretion luminosity per (fractional) area, as systems with the same value of L_f scale similarly.

One can notice two additional interesting points in these plots. First, the luminosity is not at its maximum when the line of sight is parallel to the magnetic field lines (that is, when $\mu = 1.0$ or $\gamma = 0$ degrees), which is expected because of the higher value of the optical depth in the parallel direction $\tau_\parallel$, especially in the case of a small accretion region, according to Equation 4.1. This effect is much more pronounced for the Bremsstrahlung than blackbody radiation, which makes sense as the blackbody radiation is generated in a larger area farther from the accretion stream. Second, in larger accretion regions ($f = 10^{-2}$) there is more radiation at $\mu < 0.0$ (or $\gamma > 90$ degrees, where the impact surface is not visible), since by Equation 4.1, $\tau_\parallel$ is relatively low for larger f, therefore their corresponding surface of last scattering for the photons is higher up above the WD surface, and so more photons escape to infinity at the larger viewing angles. For an observer, the viewing angle γ between the line of sight and the magnetic axis of the WD will continuously change as the WD spins with respect to the distant observer. The pattern of this variation will be determined by the geometry of the system, namely: the angle between the line of sight and the WD's rotational axis, denoted by i_{orb} (assumed to be parallel to the orbital axis of the binary), and the angle between the WD's magnetic and rotational axes, denoted by i_B. The exact relationship between the viewing angle and the orbital phase Φ (defined to vary from 0 to 1) for a given geometry is:

$$\cos(\gamma) = \cos(i_{orb})\cos(i_B) + \sin(i_{orb})\sin(i_B)\cos(2\pi\Phi) \qquad (4.2)$$

So knowing the normalized flux's dependence on the viewing angle based

on Imamura and Durisen's calculations (shown in Figure 4.3, one can use the above viewing angle relation along with the orbital phase for a given geometry to obtain normalized light curves with orbital phase by plugging the above relation into $\mathcal{L}(\mu) = \mathcal{L}(\cos\gamma)$, giving:

$$\mathcal{F}(\Phi) = \mathcal{L}(\cos\gamma) = \mathcal{L}(\cos(i_{orb})\cos(i_B) + \sin(i_{orb})\sin(i_B)\cos(2\pi\Phi)) \quad (4.3)$$

Where $\mathcal{F}(\Phi)$ is the normalized X-ray flux as a function of orbital phase Φ for a magnetic CV system of a given geometry, i_{orb} and i_B.

So to summarize, given the X-ray accretion luminosity per (fractional) area L_f, Imamura and Durisen's hydrodynamic calculations determine the dependence of the normalized flux on the viewing angle $\mathcal{L}(\cos\gamma)$. And knowing the geometry of the system through i_{orb} and i_B, one can obtain normalized soft and hard X-ray light curves with orbital phase through applying Equation 4.3. Alternatively, if one has observed X-ray light curves and spectra of a magnetic CV and wants to constrain the geometry of the system, one can generate simulated light curves based on this model for various geometries and compare them to the observed light curves. This is possible because from fitting the X-ray spectrum of the system, the X-ray accretion flux F_{acc} can be obtained, as well as an estimate of the size of the accretion region on the WD's surface. The latter is obtained from the blackbody component of the spectral fit, specifically from the blackbody normalization fit parameter called "bbodynorm" in heasoft's XSPEC bbodyrad spectral model. Here:

$$bbodynorm = R_{km}^2 / D_{10kpc}^2 \quad (4.4)$$

With R_{km} being the radius of the emitting region in km and D_{10kpc} being the source distance in the units of 10 kpc [1]. Hence an estimate of the fraction

---

[1]https://heasarc.nasa.gov/lheasoft/xanadu/xspec/manual/node137.html
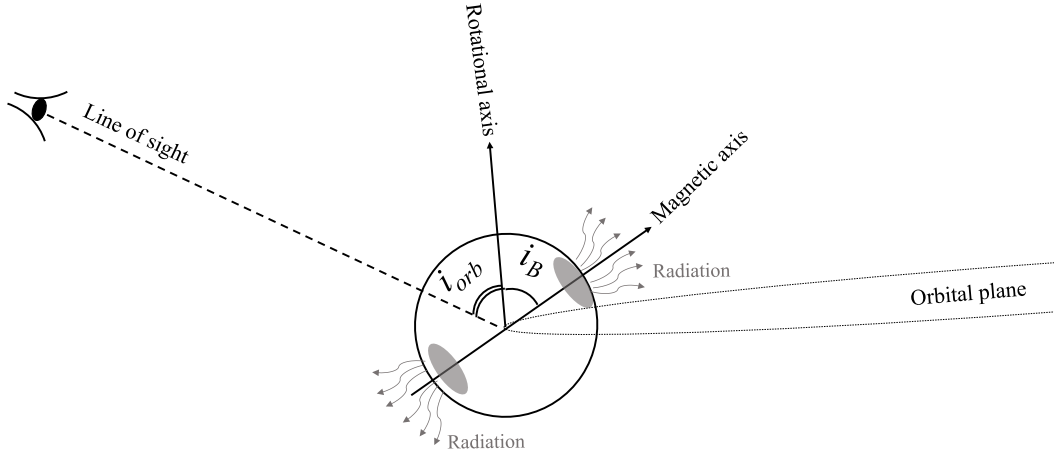
Figure 4.2: Schematic of X10's rough geometry, indicating the rotational and magnetic axes, hot spot, orbital plane, line of sight, and the two angles involved.

of the surface area of the WD occupied by the accretion region f can be made, giving an estimate of the X-ray accretion luminosity per (fractional) area L_f. And given that value, the angular dependence of the accretion flux $\mathcal{L}(\cos\gamma)$ can be determined, and consequently, the X-ray light curves $\mathcal{F}(\Phi)$ can be simulated for various geometries. This is what I have done with X10.

4.2   Setting up the simulation for X10

Following the methodology described above to roughly constrain the geometry of X10, I had to make an assumption of the mass of the WD in the system, since this value is not known yet. Following Imamura and Durisen's simulations I assumed a 1 solar mass WD, which is not an unreasonable assumption for the mass of a WD in a magnetic CV, since the mass of WDs in such systems is between 0.8 an 1.2 solar masses (Wijnen et al., 2015). And following the WD mass-radius relation from Nauenberg (1972), a WD radius of $R_{WD} \sim 6000$ km was adopted. Then we use the fitted X-ray spectrum of X10 to obtain estimates of the two observed properties of concern in this simulation: (1) The X-ray accretion luminosity L_{acc}. From the spectrum of the merged 2002

data, the flux of the photons of energies between 0.5 keV to 10 keV is $F_{acc} \sim$ 8.34×10^{-14}. Using the best estimate of the distance to 47 Tuc of $D = 4.53$ kpc from Bogdanov et al. 2016, the X-ray accretion luminosity is therefore $L_{acc} = F_{acc}.4\pi D^2 \sim 2.2 \times 10^{32}$ erg s^{-1} between 0.5-10 keV.

(2) The fraction of the surface area of the WD that the accretion region occupies f. This, as mentioned above, can be estimated from the Blackbody spectrum fit's normalization parameter according to Equation 4.4. So with bbodyrad norm= $1.60665 \times 10^{+04}$ for the merged 2002 data shown in Table 2.2, and $D_{10kpc} = 0.453$ Bogdanov et al. 2016, and approximating the accretion region as being circular, it then makes up about $f \sim$ bbodynorm. $\pi D_{10kpc}^2 / 4\pi R_{km}^2 \sim$ 4×10^{-5} of the WD's surface.

These values of L_{acc} and f for the system therefore give an accretion luminosity per fractional area of $L_f \sim 5 \times 10^{36}$ erg s^{-1}. Since systems with the same value of accretion luminosity per fractional area scale with each other, the angular dependence of the normalized accretion luminosity of X10 $\mathcal{L}(\cos\gamma)$ therefore approximately scales with that shown in Figure 4.3. I then found a piece-wise functional form via least-square fits for $\mathcal{L}(\cos\gamma)$ for $L_f \sim 5 \times 10^{36}$ and used Equation 4.2 as the argument in the resulting function for various values of i_{orb} and i_B, for both soft and hard X-rays (below and above 2 keV, respectively). The resulting simulated light curves for the various geometries are shown in Figures 4.4 and 4.5.

Then I compared the resulting simulated light curves with orbital phase, with spin-folded observed light curves of X10 for both soft and hard X-rays (with the spin period that was found from the least squares fits discussed in the previous chapter). Despite the probable asynchronism between the WD spin and binary orbital periods in X10, the simulated light curves with orbital phase and the observed light curves with spin phase should be similar, assuming a sufficiently small degree of asynchronism between the WD spin and binary orbital periods, and given that the observations subject to the comparison are

short enough not to contain a beat period envelope and/or pole-switching.

4.3 Simulation results, and comparing with observed light curves

So since in X10, $L_f \sim 5 \times 10^{36}$, it then approximately scales with $\mathcal{L}(\cos\gamma)$ shown in Figure 4 of Imamura and Durisen 1983, for which I have found a piece-wise functional form via least-square fits. I then used Equation 4.2 as the argument in our functional form of $\mathcal{L}(\cos\gamma)$ as in Equation 4.3 for various values of i_{orb} and i_B, then compared the resulting light curves with our observations.I compared the simulated light curves with observations for energies below 2 keV, and above 2 keV, though the lower-energy light curves appear to be more constraining. Figures 4.6 and 4.7 show the soft and hard spin-folded light curves from obsID 2737 superimposed on simulated light curves with $i_B = 60°$ and i_{orb} between 55° and 85°. Generally, I found that the simulation agrees best with the data at $60° \leq i_{orb} \leq 85°$ and $i_B \sim 60°$. And indeed, these rough geometry constraints are consistent with the visibility of two different accretion regions near opposite magnetic poles. One can see that in Figure 4.2, which I constructed around these limits to roughly visualize how the system is oriented with respect to us. These are very rough constraints on the geometry of the system because the simulation assumes a WD mass (and hence radius), and the parameter bbodyradnorm from which I estimated the approximate size of the accretion region has a large uncertainty. However, the WD radius estimate does not significantly affect the final value of L_f. Also note that I used information from the 2002 spectrum and not 2014/2015 because the 2002 data, with lower contamination of the ACIS detector, has much higher observed count rates, and therefore lower statistical errors (Plucinsky et al., 2016).
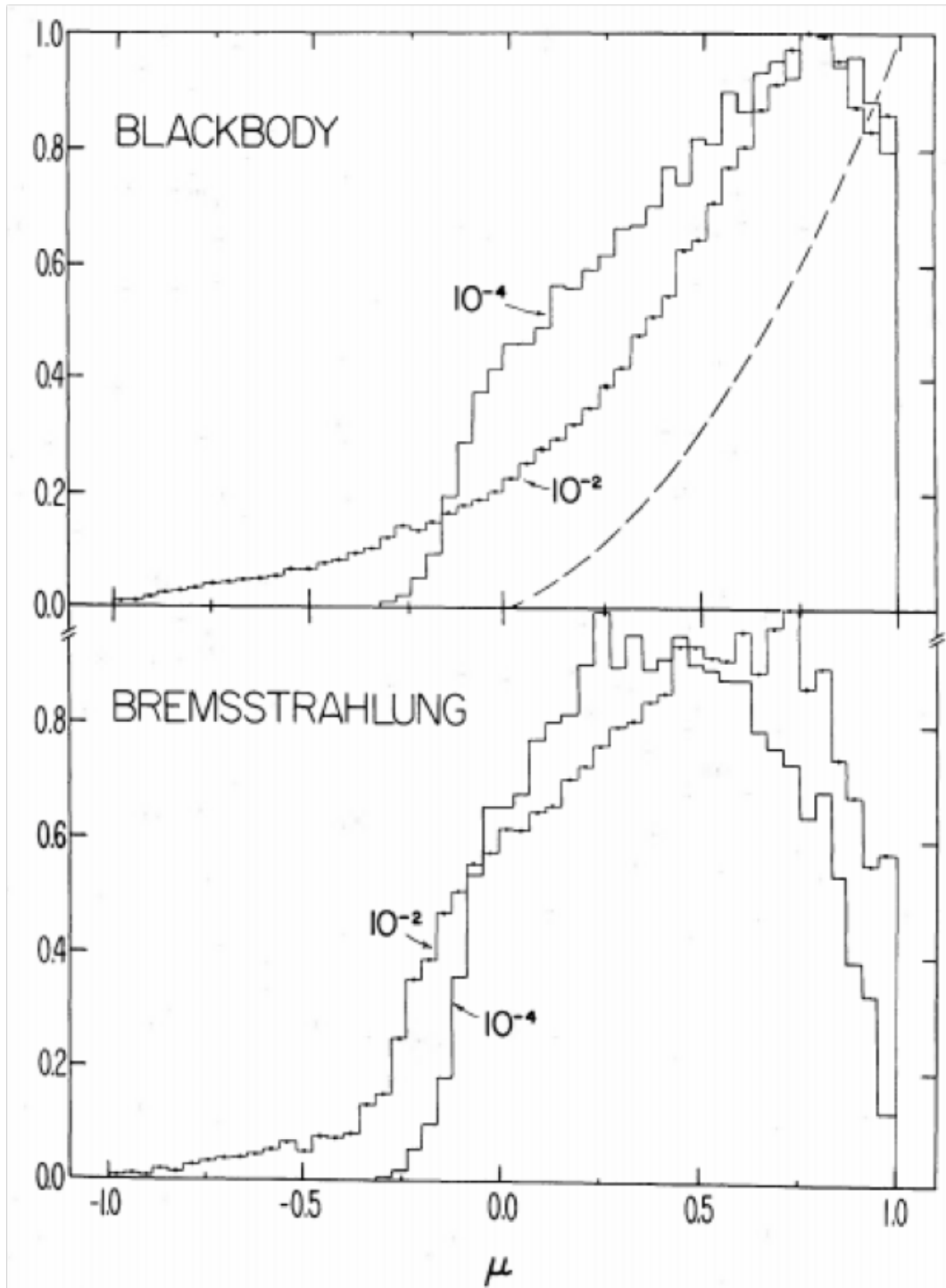
Figure 4.3: The calculated angular dependence of soft (top) and hard (bottom) X-ray emission from one accretion region on a magnetic CV, for two different choices of f (indicated) for a one solar mass WD. The y-axis shows the normalized flux observed at a certain viewing angle. And the x-axis is $\mu = \cos(\gamma)$ where γ is the viewing angle. From Imamura and Durisen (1983).
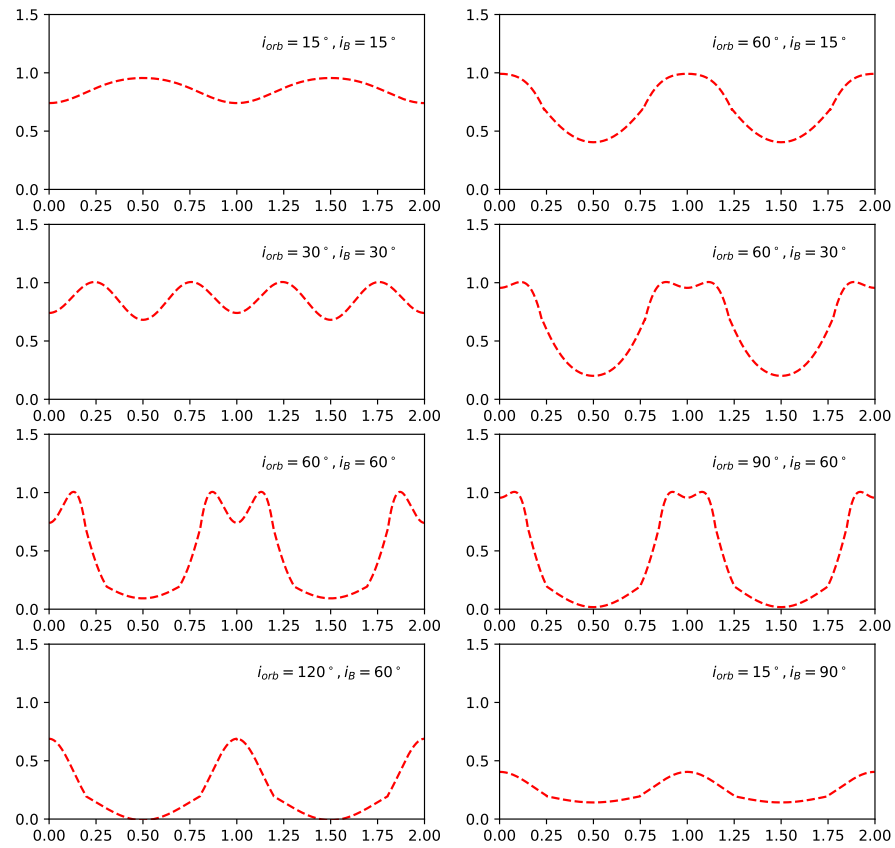
Figure 4.4: Simulations of soft X-ray light curves at various geometries.
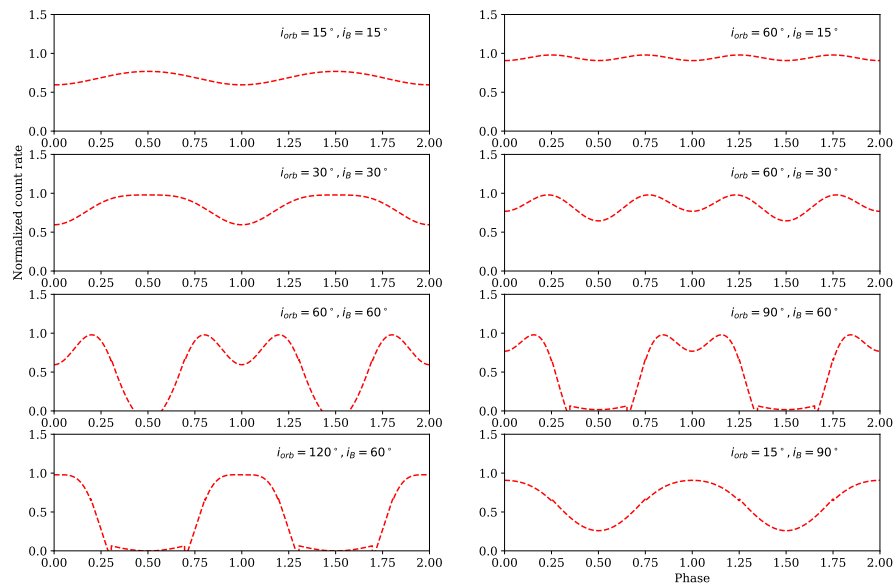
Figure 4.5: Simulations of hard X-ray light curves at various geometries.

42
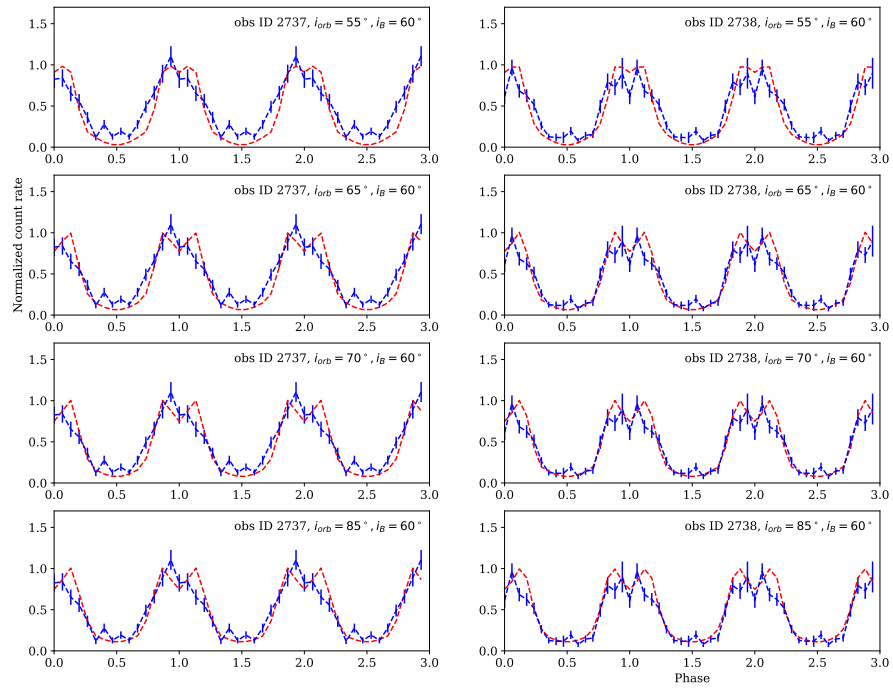
Figure 4.6: Comparison of observed soft X-ray light curves of X10 (blue dashed lines) with simulated ones (red dashed lines), for various inclinations.
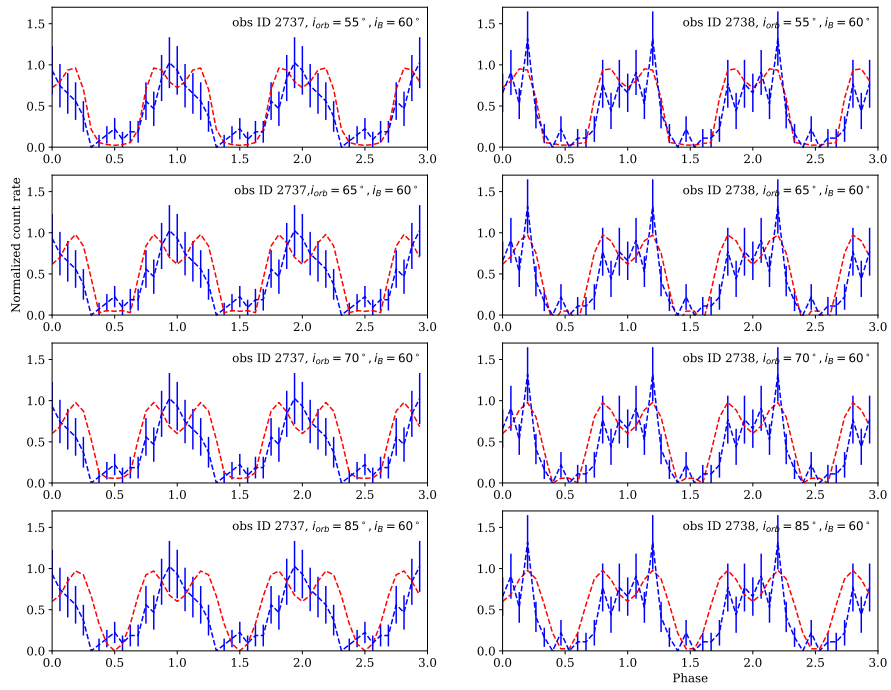
Figure 4.7: Comparison of observed hard X-ray light curves of X10 (blue dashed lines) with simulated ones (red dashed lines), for various inclinations.

Chapter 5

Trying to set limits on X10's orbital period

5.1 Understanding the pole-switching accretion

The observed phase shifts in the spin-modulated X-ray light curves of X10 are most likely caused by the accretion stream switching between two accretion regions near opposite magnetic poles of the WD. I provided evidence supporting this scenario in the previous three chapters. First (Chapters 2 and 3), there is evidence for a clear periodicity at 4.185 hours, yet in some observations there is evidence for two separate emission regions at near-opposite phases contributing to the light curve, and varying independently. Second (Chapter 4), the constraints on the system's geometry from the shape of the modulations, in comparison with theoretical calculations of the predicted shape expected from an accretion flow, predict the visibility of two accretion regions near two opposite poles.

In considering this pole-switching accretion scenario, the next thing to think about is what causes this phenomenon. The accretion stream tends to follow the magnetic field lines that lead it towards the nearest WD magnetic pole to the secondary star, hence, a pole-switching accretion implies which pole is

closest to the secondary switches regularly, due to asynchronism between the WD spin and the binary orbital period. If the WD spins at a different rate than the orbit of the binary, the orientation of the magnetic axis of the WD (if it is not parallel to the WD spin axis) with respect to the companion -and hence the accretion region nearest to the companion- will change periodically. The period at which this change occurs depends on the degree of asynchronism of the system (or the beat period,see below), specifically, the period at which the pole-switching occurs P_{env}. Assuming a dipolar magnetic field of the WD, this period is given by:

$$P_{env} = \frac{1}{2} P_{beat} \tag{5.1}$$

Where P_{beat} is the beat period, given by:

$$P_{beat} = \frac{1}{P_{spin}^{-1} - P_{orb}^{-1}} \tag{5.2}$$

The theoretical X-ray light curves for such asynchronous systems will therefore be sinusoids modulated at the spin period, with a sinusoidal amplitude envelope function modulated at half the beat period:

$$CR(t) = E(t) \sin(\frac{2\pi}{P_{spin}} t - \phi + B) \tag{5.3}$$

Where CR stands for the count rate, and the envelope function $E(t)$ is:

$$E(t) = A \sin(\frac{2\pi}{P_{env}} t - \phi) + C \tag{5.4}$$

The reason for the sinusoidal amplitude envelope at half the beat period is that as one pole moves away from the secondary, the accretion rate towards it and hence the brightness of X-ray emission will start to drop during the asynchronous rotation of the WD with the orbit. Then the accretion stream switches towards the opposite pole as it gets closer to the secondary, the accretion rate towards it, and hence the X-ray brightness at the opposite phase will

start increasing until it reaches a maximum, then drops as the first pole starts getting closer again(Wynn and King, 1992).

5.2   My rough estimate of the orbital period

The first thought I had was to try to compare the observed X-ray power spectra with ones of the simulated light curves with envelopes for various degrees of asynchronism, using Equations 5.3 and 5.4, to see which one matches best, and thus constrain the orbital period. However, that did not work since the available observations are not long enough to cover a full envelope, except for possibly the first pair of 2002 observations, which however had two opposite phases showing together within what seems to be the same envelope, along with some unexpected amplitude changes, which complicated the observed power spectrum quite a bit. Plus, the accretion regions in X10 seem to shift around on the WD surface as discussed in Chapter 3, again, creating complications in the power spectra. Both of these factors prevented me from making valid comparisons between the theoretical and observed power spectra, hence I was not able to narrow down the orbital period with this method.

My second approach was to try to roughly constrain the range of possible envelope periods matching the data, and hence, the range of possible orbital periods (since they are related by Equations 5.1 and 5.2). I investigated the range of possible envelope periods by plotting simulated light curves with the two phases and with full envelopes over the merged observed light curves following Equations 5.3 and 5.4. This was to see which envelope periods matched the apparent envelope patterns found in the second 2002 observation, and in the second and third 2005 observations. Examples of this are shown in Figures 5.1 and 5.2. After trying many different values of P_{env}, it seems that an envelope period of at least ≈ 48.31 hours is needed to match the envelope pattern of the second 2002 observation. And the envelope period matching

Figure 5.1: The simulated light curve with the two phases and with full envelopes plotted over the merged observed light curves, for $P_{env} = 56.4393$ hrs following Equations 5.3 and 5.4. Note that I chose a phase separation of $\alpha = 165°$ for these plots, which is the mid-value of the range of phase shifts found in the observed light curves, as discussed in Chapter 3.

this observation could be larger, matching it up to ≈ 114.49 hours, as shown in Figure 5.2. Notice, however, that this period does not match the apparent envelope of the 2005 observations, however, these deviations from the model could be due to irregularities in the accretion rate. In order to find the range of possible orbital periods from the range of possible envelope periods, I have solved Equations 5.1 and 5.2 for P_{orb} in terms of the envelope period:

$$P_{orb} = \left(\frac{1}{P_{spin}} - \frac{1}{2P_{env}}\right))^{-1} \tag{5.5}$$

So to find the rough range of possible orbital periods, I plotted Equation 5.5
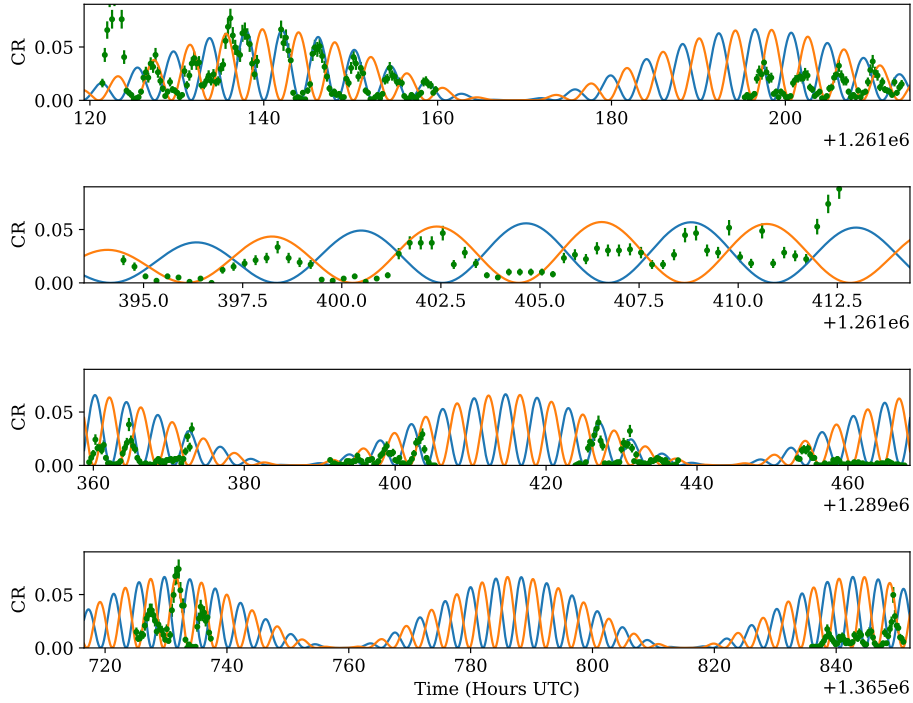
48
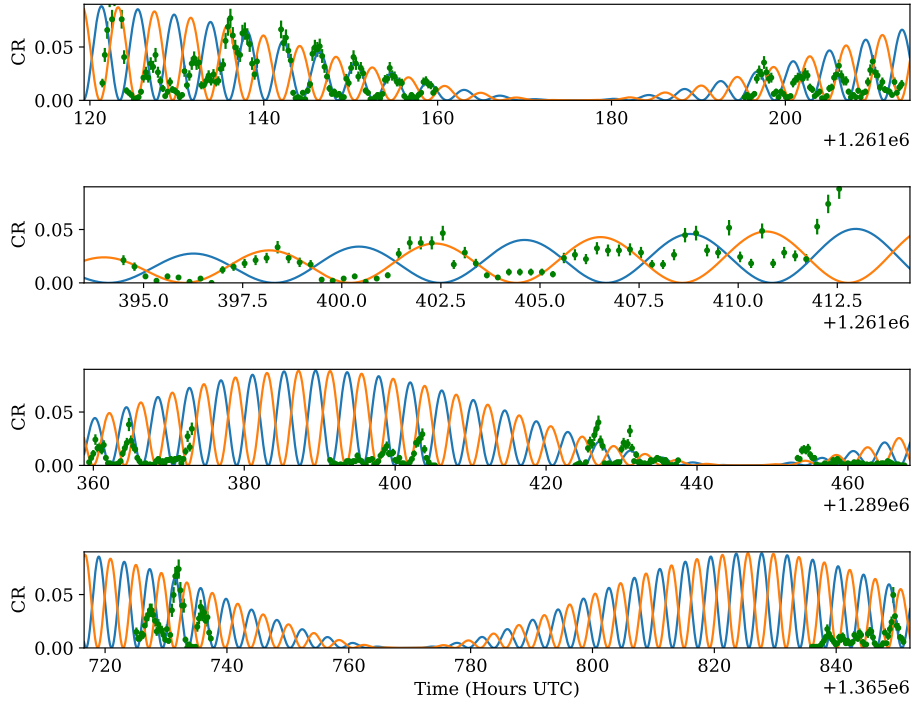
Figure 5.2: The simulated light curve with the two phases and with full envelopes plotted over the merged observed light curves, for $P_{env} = 114.4928$ following Equations 5.3 and 5.4. Note that I chose a phase separation of and $\alpha = 165°$ for these plots, which is the mid-value of the range of phase shifts found in the observed light curves, as discussed in Chapter 3.

in the range of envelope periods that I found to match the observed light curves (from 48.31 to 114.49 hours). And as one can see from Figure 5.3, the resulting range of possible orbital periods is from ≈ 4.26 to ≈ 4.37 hours, corresponding to degrees of asynchronism with the WD spin period from $\approx 1.76\%$ to $\approx 5.96\%$, respectively. In this range of possible degrees of asynchronism, X10 could be classified as either an asynchronous polar or an intermediate polar (Norton et al., 2004).

I am limited to making these rough constraints on the range of possible orbital periods because of the limited amount of observations available, the light curves of which do not show a full clear envelope, and exhibit some irregular
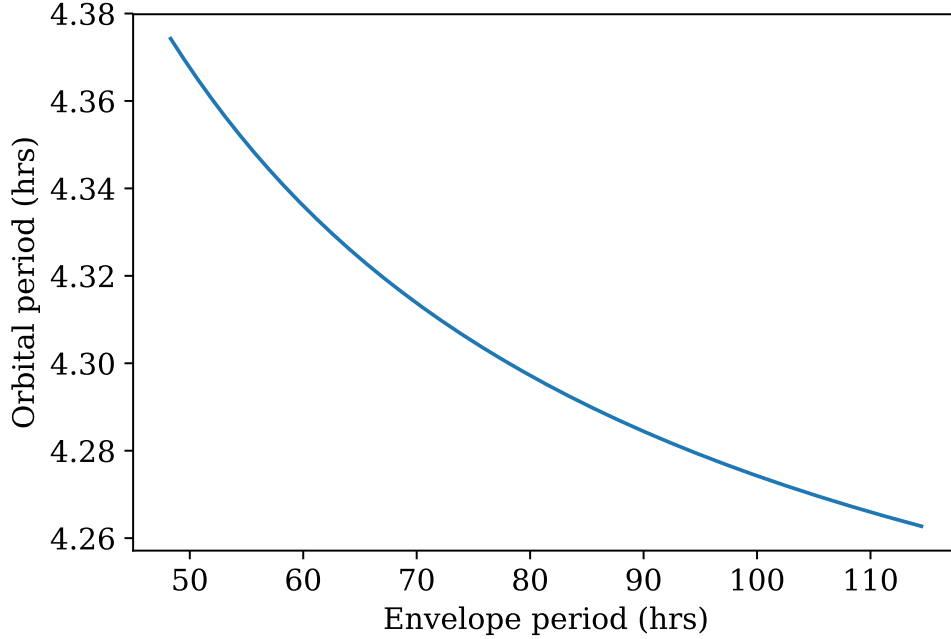
Figure 5.3: The dependence of the inferred orbital period on the envelope period, following Equation 5.5.

behaviours causing further complications in trying to find clear envelope patterns, like sudden unexpected increases in the accretion rate, both poles being active at the same time, and apparent shifting of the accretion regions on the WD surface. Better constraints on the orbital period, and hence on the degree of asynchronism and whether X10 is an asynchronous polar or an IP, could be obtained through longer X-ray observations that could provide fuller light curves with more information on the envelope. Or possibly with optical data, since the optical cyclotron radiation is modulated at the binary orbital period, though the spin and orbital signals have not yet been clearly detected in long optical datasets from the Hubble Space Telescope (Edmonds et al., 2003b).

50

5.3 Complications in fitting the light curves with this envelope model

Given the range of possible orbital periods, I could not obtain a unique set of best fit parameters to the observed light curves using Equations 5.3 and 5.4. As that there are many minima in the chi-squared space, which are often close together, but each minimum is quite sharp, so the resulting fit parameters are highly dependent on the initial guess. The reason for this is the observations are not long enough for a single orbital period to be fit uniquely to the data. Figure 5.4 shows one example of a least squares fit, for an initial orbital period guess of $P_{orb} = 4.30$ hrs, yielding the same best fit orbital period for all shown observations of $P_{orb} = 4.2988$ hrs, with errors of order 1×10^{-10} (one can see the heavy dependence of the fit orbital period on the initial guess here!).

According to this model of pole-switching accretion, the cycles within the same envelope should have the same phase. However, we see exceptions to this with the observed light curves versus the model in Figure 5.1. For example, there are two phases active together in the first 2002 observation. And the predicted envelope containing the second and third 2005 observations seems to start and end by cycles of different phases (that are separated by around $150°$ to $160°$, as shown in the light curve fits in Chapter 3). One could try to explain the two simultaneously active accretion regions through a sudden increases in the accretion rate (possibly due to higher density patches forming in the accretion stream), which increase the ram pressure of the accretion stream moving along the magnetic field lines of the WD, which in turn can cause the accretion stream to channel along the magnetic field lines leading towards the farther accretion region near the opposite pole. Thus causing both poles to be active at the same time, and so we may observe their X-ray emission within the same envelope as they move in and out of view with the spin of the WD.
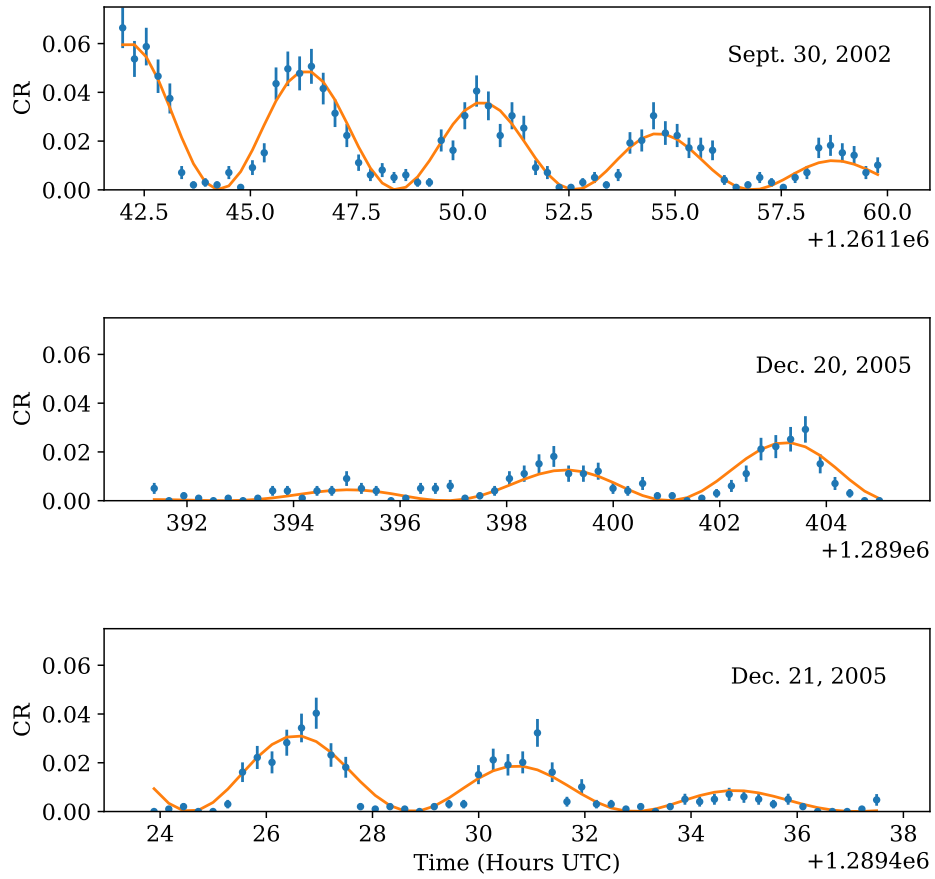
Figure 5.4: Least squares fit of light curves with an initial orbital period guess of $P_{orb} = 4.30$ hrs. Where the fit model is the orange line, and the data are the blue points.

Chapter 6

Conclusions

In this thesis, I presented my studies of Chandra X-ray data of the magnetic cataclysmic variable X10 in the globular cluster 47 Tuc, from 2002, 2005 and 2014-2015. Fitting its 2002 and 2014 X-ray spectra with a soft blackbody model and two hot plasma models including Bremsstrahlung and line emission showed that the fit parameters are consistent with X-ray spectra of polars, agreeing with previous speculations about the system.

6.1 Phase shifts in the spin modulation hinting at spin-orbit asynchronism

A first look at the X-ray light curves of X10 shows significant brightness variations, some are sudden, and others are gradual and following a smooth pattern. By taking a closer look at the patterns in the light curves, plotting periodic tick-marks starting from a fixed point showed shifting in the cycles. As the same periodic tick-marks correspond to maxima in some observations, and to minima in others. By treating the light curve modulation as sinusoidal, the transition of the cycles indicated by the periodic tick marks can be interpreted as phase shifts of the sinusoidal signal. And by interpreting the sinusoids to be

a result of an X-ray-emitting accretion region near a magnetic pole of the WD spinning in and out of our view, then the observed phase shifts of the cycles can be interpreted as a result of a pole-switching accretion. These phase shifts lead to the hypothesis that X10 is an asynchronous system. Because when the WD is spinning asynchronously with the binary orbit, the orientation of the magnetic axis of the WD with respect to the secondary will change periodically with half the spin-orbit beat period (assuming the WD's magnetic and spin axes are not parallel), causing the accretion stream to switch between magnetic poles. And that causes a phase shift in the spin modulation.

6.2 The relevant questions to find support for the asynchronism scenario

To find support (or lack thereof) to this asynchronism hypothesis with the limited X-ray data I had, I attempted to answer two main questions: (1) Could these observed phase shifts in the X-ray light curves be a result of accretion onto regions near two opposite magnetic poles; and (2) can the X-ray light curve amplitude variations give clues to an envelope pattern, and hence a beat period that could potentially constrain the system's orbital period?

6.3 The consistency of the rough geometry with two-pole visibility

To answer the first question, I attempted to set rough constraints on the system's geometry, to see if these constraints are consistent with the possibility of observing two different accretion regions near opposite magnetic poles of the WD. I did that through simulating soft and hard X-ray light curves based on the model by Imamura and Durisen (1983), which is dependent on the X-ray

accretion luminosity per (fractional) area of the accretion region L_f, on the inclination of the system with respect to us i_{orb}, and the angle between the WD's magnetic and spin axes i_B. I was able to roughly estimate the value of L_f from the X-ray spectral fit and by making a reasonable assumption on the mass — and hence size — of the WD, and then generate simulated light curves for various geometries, comparing them with observed X-ray light curves to see which geometries match them best. The resulting rough geometry constraints are $i_B = 60°$ and i_{orb} between $55°$ and $85°$, which are indeed consistent with the visibility of two opposite poles (see Figure 4.2, visualizing X10, constructed around these rough constraints).

6.4   Clues to a beat period, and roughly constraining the orbital period

Having analyzed power spectra of X10 and applied least squares fits to the light curves (as discussed in Chapter 2), I learned three major results: (1) The spin period of the WD is 4.185 ± 0.038 hours; (2) the phase shifts in the spin modulation vary between $\sim 150°$ and $\sim 180°$, which implies that the accretion regions near the magnetic poles tend to move around to a certain extent; and (3) the light curves of some observations show amplitude variations that could be a clue to a spin-orbit beat envelope pattern (e.g., obsIDs 2736, 5543 and 5544).

So knowing these results, and having more confidence in the scenario of the observed phase shifts being caused by a pole-switching accretion stream, I was able to explore the possibility of asynchronism a bit further. I did that in Chapter 5, by roughly constraining the range of possible envelope periods by trying to match simulated light curves with two phases (chosen to be separated by a middle value of $165°$, given the range of observed phase shifts mentioned in the second result above) and with full envelopes over the merged observed light

curves the light curves. And since the envelope period is that over which the accretion stream would switch towards the opposite magnetic pole, it is taken to be half the spin-orbit beat period. Hence, by roughly constraining the range of possible envelope periods by comparing to observed light curves, and knowing the WD spin period, I was able to roughly constrain the range of possible orbital periods for X10. The resulting rough range is from ≈ 4.26 to ≈ 4.37 hours, which in turn correspond to degrees of asynchronism from $\approx 1.76\%$ to $\approx 5.96\%$. Within this range of degrees of asynchronism, X10 could either be an asynchronous polar, or a diskless intermediate polar. Optical data, or longer X-ray observations revealing full envelopes would greatly improve these constraints of the degree of asynchronism, and may favour one classification of X10 over the other.

6.5   Final remarks

In this thesis, I tried to get the most information I could from the limited data I had on X10 in the X-rays alone. And while my estimates of X10's geometry using the simulations from Imamura and Durisen (1983) are rough due to the assumptions I had to make and errors in the spectral fit, the same analysis approach could be applied to other magnetic cataclysmic variables. And the geometry results can have better accuracy if the mass of the WD of the system is known, and the X-ray spectral fits are more accurate. In addition, if a mCV has been observed for a long time period, one might try applying this analysis on data over the years to try to see if there are any noticeable changes in the accretion geometry, which could be beneficial for the studies of the evolution of binary systems and the magnetic interactions within them. Finally, the same applies to my analysis trying to roughly estimate the range of possible orbital periods from limited X-ray light curves, through envelope period analysis: if an asynchronous mCV has longer observations with more clear envelopes, better

constraints on the orbital period could be obtained from just the X-ray light curves.

Bibliography

M. Auriere, L. Koch-Miramond, and S. Ortolani. The X-ray source in the core of 47 Tucanae. *A&A*, 214:113–122, April 1989.

A. Bahramian, C. O. Heinke, V. Tudor, J. C. A. Miller-Jones, S. Bogdanov, T. J. Maccarone, C. Knigge, G. R. Sivakoff, L. Chomiuk, J. Strader, J. A. Garcia, and T. Kallman. The ultracompact nature of the black hole candidate X-ray binary 47 Tuc X9. *MNRAS*, 467:2199–2216, May 2017. doi: 10.1093/mnras/stx166.

F. Bernardini, D. de Martino, K. Mukai, M. Falanga, I. Andruchow, J.-M. Bonnet-Bidaud, N. Masetti, D. H. G. Buitrago, M. Mouchet, and G. Tovmassian. On the nature of the hard X-ray sources SWIFT J1907.3-2050, IGR J12123-5802 and IGR J19552+0044. *MNRAS*, 435:2822–2834, November 2013. doi: 10.1093/mnras/stt1434.

S. Bogdanov, C. O. Heinke, F. Özel, and T. Güver. Neutron Star Mass-Radius Constraints of the Quiescent Low-mass X-Ray Binaries X7 and X5 in the Globular Cluster 47 Tuc. *ApJ*, 831:184, November 2016. doi: 10.3847/0004-637X/831/2/184.

C. G. Campbell. Spin evolution of magnetic white dwarfs in AM Herculis binaries. *MNRAS*, 211:69–74, November 1984. doi: 10.1093/mnras/211.1.69.

G. W. Clark. X-ray binaries in globular clusters. *ApJ*, 199:L143–L145, August 1975. doi: 10.1086/181869.

R. Connon Smith. Cataclysmic Variables. *arXiv Astrophysics e-prints*, January 2007.

M. Cropper. The Polars. *Space Sci. Rev.*, 54:195–295, December 1990. doi: 10.1007/BF00177799.

P. D. Edmonds, R. L. Gilliland, C. O. Heinke, and J. E. Grindlay. An Extensive Census of Hubble Space Telescope Counterparts to Chandra X-Ray Sources in the Globular Cluster 47 Tucanae. II. Time Series and Analysis. *ApJ*, 596: 1197–1219, October 2003a. doi: 10.1086/378194.

P. D. Edmonds, R. L. Gilliland, C. O. Heinke, and J. E. Grindlay. An Extensive Census of Hubble Space Telescope Counterparts to Chandra X-Ray Sources in the Globular Cluster 47 Tucanae. I. Astrometry and Photometry. *ApJ*, 596:1177–1196, October 2003b. doi: 10.1086/378193.

G. P. Garmire, M. W. Bautz, P. G. Ford, J. A. Nousek, and G. R. Ricker, Jr. Advanced CCD imaging spectrometer (ACIS) instrument on the Chandra X-ray Observatory. In J. E. Truemper and H. D. Tananbaum, editors, *X-Ray and Gamma-Ray Telescopes and Instruments for Astronomy.*, volume 4851 of *Proc. SPIE*, pages 28–44, March 2003. doi: 10.1117/12.461599.

R. D. Geckeler and R. Staubert. Periodic changes of the accretion geometry in the nearly-synchronous polar RX J1940.1-1025. *A&A*, 325:1070–1076, September 1997.

J. E. Grindlay, C. Heinke, P. D. Edmonds, and S. S. Murray. High-Resolution X-ray Imaging of a Globular Cluster Core: Compact Binaries in 47Tuc. *Science*, 292:2290–2295, June 2001. doi: 10.1126/science.1061135.

J. P. Halpern, S. Bogdanov, and J. R. Thorstensen. X-Ray and Optical Study of the Gamma-ray Source 3FGL J0838.8-2829: Identification of a Candidate

Millisecond Pulsar Binary and an Asynchronous Polar. *ApJ*, 838:124, April 2017. doi: 10.3847/1538-4357/838/2/124.

G. Hasinger, H. M. Johnston, and F. Verbunt. Discovery of multiple X-ray sources in 47 Tucanae. *A&A*, 288:466–471, August 1994.

C. O. Heinke, J. E. Grindlay, D. A. Lloyd, and P. D. Edmonds. X-Ray Studies of Two Neutron Stars in 47 Tucanae: Toward Constraints on the Equation of State. *ApJ*, 588:452–463, May 2003. doi: 10.1086/374039.

C. O. Heinke, J. E. Grindlay, P. D. Edmonds, H. N. Cohn, P. M. Lugger, F. Camilo, S. Bogdanov, and P. C. Freire. A Deep Chandra Survey of the Globular Cluster 47 Tucanae: Catalog of Point Sources. *ApJ*, 625:796–824, June 2005. doi: 10.1086/429899.

C. O. Heinke, R. Wijnands, H. N. Cohn, P. M. Lugger, J. E. Grindlay, D. Pooley, and W. H. G. Lewin. Faint X-Ray Sources in the Globular Cluster Terzan 5. *ApJ*, 651:1098–1111, November 2006. doi: 10.1086/507884.

C. Hellier and A. P. Beardmore. The accretion flow in the discless intermediate polar V2400 Ophiuchi. *MNRAS*, 331:407–416, March 2002. doi: 10.1046/j.1365-8711.2002.05199.x.

P. Hertz and J. E. Grindlay. An X-ray survey of globular clusters and their X-ray luminosity function. *ApJ*, 275:105–119, December 1983. doi: 10.1086/161516.

J. N. Imamura and R. H. Durisen. X-ray spectra and light curves of accreting magnetic degenerate dwarfs. *ApJ*, 268:291–308, May 1983. doi: 10.1086/160954.

A. Jordán, P. Côté, L. Ferrarese, J. P. Blakeslee, S. Mei, D. Merritt, M. Milosavljević, E. W. Peng, J. L. Tonry, and M. J. West. The ACS Virgo Cluster Survey. III. Chandra and Hubble Space Telescope Observations of

Low-Mass X-Ray Binaries and Globular Clusters in M87. *ApJ*, 613:279–301, September 2004. doi: 10.1086/422545.

A. Joshi, J. C. Pandey, K. P. Singh, and P. C. Agrawal. PALOMA: A Magnetic CV between Polars and Intermediate Polars. *ApJ*, 830:56, October 2016. doi: 10.3847/0004-637X/830/2/56.

D. Koester and G. Chanmugam. REVIEW: Physics of white dwarf stars. *Reports on Progress in Physics*, 53:837–915, July 1990. doi: 10.1088/0034-4885/53/7/001.

E. Kuulkers, A. Norton, A. Schwope, and B. Warner. *X-rays from cataclysmic variables*, pages 421–460. April 2006.

D. A. Liedahl, A. L. Osterheld, and W. H. Goldstein. New calculations of Fe L-shell X-ray spectra in high-temperature plasmas. *ApJ*, 438:L115–L118, January 1995. doi: 10.1086/187729.

Y. M. Lipkin and E. M. Leibowitz. V4633 Sgr - a probable second asynchronous polar classical nova. *MNRAS*, 387:289–294, June 2008. doi: 10.1111/j.1365-2966.2008.13217.x.

P. A. Mason, G. Ramsay, I. Andronov, S. Kolesnikov, N. Shakhovskoy, and E. Pavlenko. Evidence for pole switching in the magnetic cataclysmic variable BY Camelopardalis. *MNRAS*, 295:511, April 1998. doi: 10.1046/j.1365-8711.1998.01185.x.

G. Meylan and D. C. Heggie. Internal dynamics of globular clusters. *A&ARv*, 8:1–143, 1997. doi: 10.1007/s001590050008.

J. C. A. Miller-Jones, J. Strader, C. O. Heinke, T. J. Maccarone, M. van den Berg, C. Knigge, L. Chomiuk, E. Noyola, T. D. Russell, A. C. Seth, and G. R. Sivakoff. Deep radio imaging of 47 Tuc identifies the peculiar X-ray

source X9 as a new black hole candidate. *MNRAS*, 453:3918–3931, November 2015. doi: 10.1093/mnras/stv1869.

S. S. Murray, G. K. Austin, J. H. Chappell, J. J. Gomes, A. T. Kenter, R. P. Kraft, G. R. Meehan, M. V. Zombeck, G. W. Fraser, and S. Serio. In-flight performance of the Chandra high-resolution camera. In J. E. Truemper and B. Aschenbach, editors, *X-Ray Optics, Instruments, and Missions III*, volume 4012 of *Proc. SPIE*, pages 68–80, July 2000. doi: 10.1117/12.391591.

G. Myers, J. Patterson, E. de Miguel, F.-J. Hambsch, B. Monard, G. Bolt, J. McCormick, R. Rea, and W. Allen. Resynchronization of the Asynchronous Polar CD Ind. *PASP*, 129(4):044204, April 2017. doi: 10.1088/1538-3873/aa54a8.

M. Nauenberg. Analytic Approximations to the Mass-Radius Relation and Energy of Zero-Temperature Stars. *ApJ*, 175:417, July 1972. doi: 10.1086/151568.

A. J. Norton, R. V. Somerscales, and G. A. Wynn. REVIEW: The Spin Periods of Magnetic Cataclysmic Variables. In S. Vrielmann and M. Cropper, editors, *IAU Colloq. 190: Magnetic Cataclysmic Variables*, volume 315 of *Astronomical Society of the Pacific Conference Series*, page 216, December 2004.

B. Paczyński. Evolutionary Processes in Close Binary Systems. *ARA&A*, 9: 183, 1971. doi: 10.1146/annurev.aa.09.090171.001151.

F. Paresce, G. de Marchi, and F. R. Ferraro. Possible cataclysmic variable in the core of the globular cluster 47 Tucanae. *Nature*, 360:46–48, November 1992. doi: 10.1038/360046a0.

J. Patterson. The DQ Herculis stars. *PASP*, 106:209–238, March 1994. doi: 10.1086/133375.

E. P. Pavlenko, P. A. Mason, A. A. Sosnovskij, S. Y. Shugarov, J. V. Babina, K. A. Antonyuk, M. V. Andreev, N. V. Pit, O. I. Antonyuk, and A. V. Baklanov. Asynchronous polar V1500 Cyg: orbital, spin, and beat periods. *MNRAS*, 479:341–347, September 2018. doi: 10.1093/mnras/sty1494.

P. P. Plucinsky, A. Bogdan, G. Germain, and H. L. Marshall. The evolution of the ACIS contamination layer over the 16-year mission of the Chandra X-ray Observatory. In *Space Telescopes and Instrumentation 2016: Ultraviolet to Gamma Ray*, volume 9905 of *Proc. SPIE*, page 990544, July 2016. doi: 10.1117/12.2233837.

D. Pooley and P. Hut. Dynamical Formation of Close Binaries in Globular Clusters: Cataclysmic Variables. *ApJ*, 646:L143–L146, August 2006. doi: 10.1086/507027.

D. Pooley, W. H. G. Lewin, S. F. Anderson, H. Baumgardt, A. V. Filippenko, B. M. Gaensler, L. Homer, P. Hut, V. M. Kaspi, J. Makino, B. Margon, S. McMillan, S. Portegies Zwart, M. van der Klis, and F. Verbunt. Dynamical Formation of Close Binary Systems in Globular Clusters. *ApJ*, 591:L131–L134, July 2003. doi: 10.1086/377074.

G. Ramsay, D. A. H. Buckley, M. Cropper, and M. K. Harrop-Allin. RX J2115-5840: confirmation of a new near-synchronous polar. *MNRAS*, 303:96–100, February 1999. doi: 10.1046/j.1365-8711.1999.02213.x.

G. Ramsay, M. Cropper, K. O. Mason, F. A. Córdova, and W. Priedhorsky. XMM-Newton observations of three short-period polars: V347 Pav, GG Leo and EU UMa. *MNRAS*, 347:95–100, January 2004. doi: 10.1111/j.1365-2966.2004.07242.x.

L. E. Rivera-Sandoval, M. van den Berg, C. O. Heinke, H. N. Cohn, P. M. Lugger, P. Freire, J. Anderson, A. M. Serenelli, L. G. Althaus, A. M. Cool, J. E. Grindlay, P. D. Edmonds, R. Wijnands, and N. Ivanova. Discovery of

near-ultraviolet counterparts to millisecond pulsars in the globular cluster 47 Tucanae. *MNRAS*, 453:2707–2717, November 2015. doi: 10.1093/mnras/stv1810.

L. E. Rivera Sandoval, M. van den Berg, C. O. Heinke, H. N. Cohn, P. M. Lugger, J. Anderson, A. M. Cool, P. D. Edmonds, R. Wijnands, N. Ivanova, and J. E. Grindlay. New cataclysmic variables and other exotic binaries in the globular cluster 47 Tucanae*. *MNRAS*, 475:4841–4867, April 2018. doi: 10.1093/mnras/sty058.

R. Schwarz, A. D. Schwope, A. Staude, A. Rau, G. Hasinger, T. Urrutia, and C. Motch. Paloma (RX J0524+42): the missing link in magnetic CV evolution? *A&A*, 473:511–521, October 2007. doi: 10.1051/0004-6361:20077684.

M. M. Shara, L. E. Bergeron, R. L. Gilliland, A. Saha, and L. Petro. Cataclysmic and Close Binaries in Star Clusters. IV. The Unexpectedly Low Number of Erupting Dwarf Novae Detected by the Hubble Space Telescope in the Core of 47 Tucanae. *ApJ*, 471:804, November 1996. doi: 10.1086/178008.

A. Silber, H. V. Bradt, M. Ishida, T. Ohashi, and R. A. Remillard. H0538 + 608 (= BY Camelopardalis) - an asynchronously rotating AM Herculis binary? *ApJ*, 389:704–713, April 1992. doi: 10.1086/171243.

H. S. Stockman, G. D. Schmidt, and D. Q. Lamb. V1500 Cygni - Discovery of a magnetic nova. *ApJ*, 332:282–286, September 1988. doi: 10.1086/166652.

G. Tovmassian, D. González-Buitrago, J. Thorstensen, E. Kotze, H. Breytenbach, A. Schwope, F. Bernardini, S. V. Zharikov, M. S. Hernandez, D. A. H. Buckley, E. de Miguel, F.-J. Hambsch, G. Myers, W. Goff, D. Cejudo, D. Starkey, T. Campbell, J. Ulowetz, W. Stein, P. Nelson, D. E. Reichart, J. B. Haislip, K. M. Ivarsen, A. P. LaCluyze, J. P. Moore, and A. S. Miroshnichenko. IGR J19552+0044: A new asynchronous short period polar. Filling

the gap between intermediate and ordinary polars. *A&A*, 608:A36, December 2017. doi: 10.1051/0004-6361/201731323.

J. VanderPlas, A. J. Connolly, Z. Ivezic, and A. Gray. Introduction to astroML: Machine learning for astrophysics. In *Proceedings of Conference on Intelligent Data Understanding (CIDU), pp. 47-54, 2012.*, pages 47–54, October 2012. doi: 10.1109/CIDU.2012.6382200.

F. Verbunt and G. Hasinger. Nine X-ray sources in the globular cluster 47 Tucanae. *A&A*, 336:895–901, August 1998.

F. Verbunt, J. van Paradijs, and R. Elson. X-ray sources in globular clusters. *MNRAS*, 210:899–914, October 1984. doi: 10.1093/mnras/210.4.899.

T. P. G. Wijnen, M. Zorotovic, and M. R. Schreiber. White dwarf masses in cataclysmic variables. *A&A*, 577:A143, May 2015. doi: 10.1051/0004-6361/201323018.

G. A. Wynn and A. R. King. Theoretical X-ray power spectra of intermediate polars. *MNRAS*, 255:83–91, March 1992. doi: 10.1093/mnras/255.1.83.